Computers and Fluids 254 (2023) 105809

Contents lists available at ScienceDirect

Computers and Fluids

journal homepage: www.elsevier.com/locate/compfluid

RANS thermal modelling of a natural convection boundary layer at low Prandtl number

Agustín Villa Ortiz [a,*], Lilla Koloszar [b]

[a] GISAT, Universidad Rey Juan Carlos, Camino del Molino nº 5, Fuenlabrada 28942, Madrid, Spain
[b] von Karman Institute for Fluid Dynamics, Waterloosesteenweg 72, Sint-Genesius-Rode 1640 Belgium

ARTICLE INFO

Keywords:
Natural convection boundary layer
Turbulence modelling
Low Prandtl fluid
Reynolds Averaged Navier–Stokes

ABSTRACT

The present work evaluates the performance of different RANS turbulence models in a natural convection boundary layer at three different Prandtl numbers: 0.71, 0.2 and 0.025. An assessment on the prediction of the boundary layer is presented in function of the wall fluxes, mean and turbulent flow fields. It is observed that the chosen turbulence model to close the momentum equation is relevant in order to capture the flow field at low Prandtl numbers. This is due to the strong interaction between the momentum and thermal fields in natural convection. From the thermal point of view, the analogy between the turbulent momentum and turbulent thermal diffusivities presents serious issues to correctly predict the flow field independently of the Prandtl number. Advanced models that employ algebraic or transport equations of the turbulent heat fluxes introduces the needed physics to correctly predict the natural convection boundary layer.

1. Introduction

Natural convection flows are driven by buoyancy forces. These forces are originated by the gravitational acceleration g and density variations (due to changes in the temperature field or species concentration). Both momentum and thermal (or species concentration) transport phenomena are coupled. The natural convection boundary layer flow (NCBL) along a heating vertical wall is shown in Fig. 1. As one can observe, the wall normal vector and the gravity direction are perpendicular. The fluid layers close to the wall are heated, and their density decreases. The hot fluid will move in the opposite direction of gravity, and it is replaced by cold particles. The flow develops due to the heat applied in the wall with length L. The fluid ascends from the bottom, and the boundary layer grows. At the beginning, this boundary layer has a laminar behaviour, but at a certain location, disturbances eventually grow, and the transition regime is established. Further, these disturbances entirely break the laminar flow, which turns turbulent. The boundary layer growing rate increases with respect to the laminar state. In this article, only the turbulent region will be considered.

The heat transfer mechanisms between the wall and the fluid are affected by the Prandtl number value, as constated by Bejan [1]. This number is defined as:

$$Pr = \frac{\nu}{\alpha} \tag{1}$$

where ν is the kinematic viscosity and α is the thermal diffusivity of the fluid. Fig. 2 shows the effect of the Prandtl number on the NCBL development. The thicknesses of the momentum and the thermal boundary layers (δ and δ_T) varies accordingly with the Prandtl number. In the case of low Prandtl numbers ($Pr < 1$), thermal diffusion is more relevant than the viscous one, and it determines the boundary layer thickness value δ. A maximum velocity location δ_U is also found within the boundary layer as velocity goes to zero at the edge of the boundary layer due to the absence of buoyancy forces. When increasing the Prandtl number beyond the unity ($Pr > 1$), the viscous effects become more important than the thermal ones, and the boundary layer thickness differ from the thermal boundary layer δ_T. Even slightly out of the thermal boundary layer, where there are no buoyancy forces, motion exists because of the strong momentum diffusion.

Natural convection flows are found in nature and engineering processes. Air circulation in HVAC is a common application, whose Prandtl number is considered as $Pr = 0.71$. Lower Prandtl number values are found in other scenarios, like in thermoacoustics [3], where noble gases are mixtured to improve the performance of thermoacoustic engines. In the case of a mixture of Helium and Xenon the Prandtl number can be decreased up to $Pr = 0.2$. Even further, the development of heavy liquid metal reactors (HLMR) considers much lower Prandtl numbers [4], such as the one of liquid Lead-Bismuth Eutectic ($Pr = 0.025$) or sodium ($Pr = 0.006$). For these reactors, natural convection is employed as a passive cooling mechanism in case of failure or maintenance scenarios. Also, the stellar fluid dynamics is governed by a Prandtl number below

* Corresponding author.
E-mail addresses: agustin.villa@urjc.es (A. Villa Ortiz), koloszar@vki.ac.be (L. Koloszar).

https://doi.org/10.1016/j.compfluid.2023.105809
Received 8 September 2022; Received in revised form 21 December 2022; Accepted 30 January 2023
Available online 2 February 2023

Nomenclature

Acronyms

AHFM	Algebraic Heat Flux Model
CFD	Computational Fluid Dynamics
DNS	Direct Numerical Simulation
EB-DFM	Elliptic Blending Differential Flux Model
EB-RSM	Elliptic Blending Reynolds Stress Model
HLMR	Heavy Liquid Metal Reactors
LES	Large Eddy Simulation
NCBL	Natural Convection Boundary Layer
RA	Reynolds analogy
RANS	Reynolds Averaged Navier–Stokes
SGDH	Simple Gradient Diffusion Hypothesis
THFM	Turbulent Heat Flux Model
TMFM	Turbulent Momentum Flux Model

Latin symbols

C_f	Skin friction coefficient
C_p	Heat capacity at constant pressure
g	Gravitational acceleration
h	Convective heat transfer coefficient
k	Turbulent kinetic energy
k_θ	Temperature variance
L	Length
L^*	Dimensionless length
L_b	Characteristic length
$\dot{m}$	Mass flow
N_x, N_y	Number of cells in specified direction
Nu	Nusselt number
P	Kinematic pressure
p	Pressure
Pr	Prandtl number
Pr_t	Turbulent Prandtl number
Ra	Rayleigh number
T	Temperature
ΔT	Temperature difference
T_τ	Friction temperature
T_∞	Far field temperature
T_{ref}	Reference temperature
T_w	Wall temperature
U, V, U_i	Velocity components
u_τ	Friction velocity
u_b	Characteristic velocity
$\overline{u'T'}$, $\overline{v'T'}$, $\overline{u_j'T'}$	Turbulent heat flux components
$\overline{u_i'u_j'}$	Reynolds stress components
x, y, z, x_i	Cartesian coordinates

Greek symbols

α	Thermal diffusivity
α_t	Turbulent thermal diffusivity
β	Thermal expansion coefficient
δ	Boundary layer thickness
δ_T	Thermal boundary layer thickness
δ_U	Maximum velocity location
ε	Turbulent kinetic energy dissipation rate
ε_θ	Temperature variance dissipation rate
ϵ_ϕ	Deviation of field ϕ with respect to a reference quantity
ν	Kinematic viscosity
ν_t	Eddy viscosity
ρ	Density
ρ_k	Kinematic density
ρ_{ref}	Reference density
τ_w	Wall shear stress

Subscript

ff	Far field patch
i, j, k	Index of component/coordinate
$inlet$	Inlet patch
$outlet$	Outlet patch
w	Field value at the wall

Superscript

$+$	Dimensionless quantity based on the law of the wall
$-$	Reynolds averaged quantity

10^{-5} [5] because of the large radiative diffusion contribution on the thermal transport.

The nature of the previous flows is marked by a turbulent behaviour. Using Computational Fluid Dynamics it is possible to analyse these flows and extract enough information to improve the state of the art of low Prandtl number fluids and the design of facilities that use them. However, simulating all the physics involved on the HMLR operation, stellar fluid dynamics… requires a very large computational cost. Therefore, researchers rely on Reynolds Averaged Navier–Stokes (RANS) simulations where all the turbulence effects are modelled in both momentum and thermal equations. The turbulence models are divided into two categories in the present work:

- turbulent momentum flux (TMF) models: which consider the effects of turbulence on the mean momentum transport equation.
- turbulent heat flux (THF) models: which consider the effects of turbulence in the mean thermal transport equation.

Turbulent momentum flux models have been widely studied in the past for several fluid and flow conditions. However, the development and knowledge of THF models is limited. Most of the commercial codes rely on analogies between the turbulent momentum-thermal behaviour. This approach, which is accepted for moderate and high Prandtl number fluids as air and water ($Pr = 7$), is not accurate when predicting the thermal behaviour of low Prandtl number fluids.

The current work contributes to the validation of RANS THF models. In Europe, the research on such models has been linked to EU collaborative projects as THINS, MYRTE or SESAME [6] to support the progress of HLMR's. Mostly based on high fidelity simulations, RANS THF models have been assessed and compared in simple flow fields at low Prandtl numbers such as channel flows [7], impinging [8] or coaxial jets [9] and backward facing steps [10]. Shams summarizes all the work along these projects [11] and shows that a great effort was done when modelling forced convection flows. However, there is a lack of development, verification and validation of THF models in natural convection for close to unity and low Prandtl numbers. Dehoux et al. [12], Da Vià et al. [13] and Shams et al. [14] studied and calibrated their respective turbulent heat flux models in natural and mixed convection conditions, though the flow was restricted to confined domains.

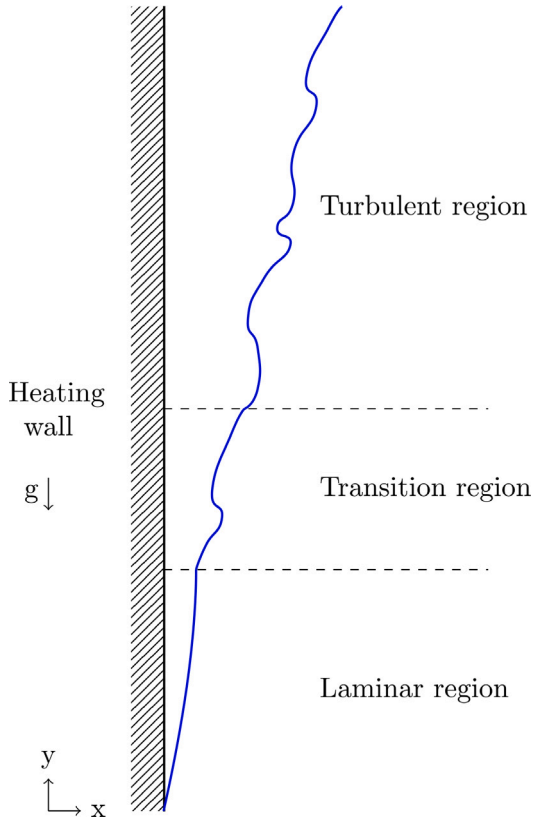

Fig. 1. Velocity boundary layer for a natural convection flow over a vertical heating plate.

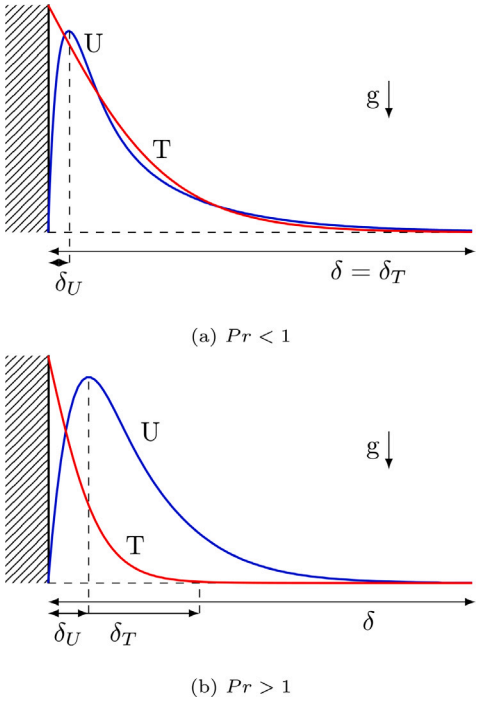

Fig. 2. Momentum (blue) and thermal (red) boundary layers of a natural convection boundary layer. The boundary layer thickness δ is presented together with the thermal boundary layer thickness δ_T and the maximum velocity location δ_U. Based on equations of Bejan [1] and analytical approximation of Bachiri [2].

The present work assess several pairs of RANS TMF-THF models in an unconfined natural convection boundary layer (NCBL). The objective of these simulations is to find a combination of RANS models that ensures a good prediction of the NCBL when low Prandtl number fluids are considered.

2. State of the art

2.1. RANS equations

The proposed simulations in this work are performed with the RANS equations. For a steady state, incompressible NCBL with constant material properties, the governing equations result in:

$$\frac{\partial \overline{U_i}}{\partial x_i} = 0 \tag{2}$$

$$\frac{\partial \overline{U_i}\,\overline{U_j}}{\partial x_j} = -\frac{\partial \overline{P}}{\partial x_i} + \nu \frac{\partial^2 \overline{U_i}}{\partial x_j^2} - \frac{\partial \overline{u_i' u_j'}}{\partial x_j} + \rho_k g_i \tag{3}$$

$$\frac{\partial \overline{U_j}\,\overline{T}}{\partial x_j} = \alpha \frac{\partial^2 \overline{T}}{\partial x_j^2} - \frac{\partial \overline{u_j' T'}}{\partial x_j} \tag{4}$$

where the field $\overline{\phi}$ denotes the ensemble average of the ϕ field. $\overline{P} = \overline{p}/\rho_{ref}$ is the kinematic pressure. The Boussinesq approximation is employed to consider the buoyancy effects in the momentum equation, being $\rho_k = \left[1 - \beta\left(\overline{T} - T_{ref}\right)\right]$ the kinematic density and β the thermal expansion coefficient.

The RANS equations predict the mean velocity $\overline{U}$ and temperature $\overline{T}$ fields. The Reynolds stresses $\overline{u_i' u_j'}$ and turbulent heat fluxes $\overline{u_j' T'}$ take into account the effect of turbulence in the mean flow field. They are modelled by the TMF and THF models, respectively.

2.2. RANS turbulent momentum flux modelling

The Reynolds stress tensor introduces the effects of turbulence in the mean momentum equation. The most usual modelling of this tensor is through the Boussinesq assumption:

$$\overline{u_i' u_j'} = -2\nu_t \left(\frac{\partial \overline{U_i}}{\partial x_j} + \frac{\partial \overline{U_j}}{\partial x_i}\right) + \frac{2}{3} k \delta_{ij} \tag{5}$$

being ν_t the eddy viscosity, and k the turbulent kinetic energy. Due to the presence of buoyancy forces, Kenjereš et al. [15], Manceau [16] and Jameel [17] propose the addition of the term:

$$-C_\theta \tau \beta \left(g_i \overline{u_j' T'} + g_j \overline{u_i' T'} - \frac{2}{3} g_k \overline{u_k' T'} \delta_{ij}\right) \tag{6}$$

to the Reynolds stress of Eq. (5). In this work, the low Reynolds $k-\varepsilon$ model of Launder and Sharma (LS) is used to obtain ν_t [18] by solving the transport equations for k and its dissipation rate ε. The effects of buoyancy are also considered in the production of k and ε thanks to the production term:

$$\mathcal{P}_{bk} = -\beta g_i \overline{u_i' T'} \tag{7}$$

$$\mathcal{P}_{b\varepsilon} = C_\varepsilon{}^* \frac{\varepsilon}{k} max\left(\mathcal{P}_{bk}, 0\right) \tag{8}$$

where $C_\varepsilon{}^*$ is defined by Henkes et al. [19].

Additionally, a differential Reynolds Stress Model has been employed in this study. These models are characterized by solving the transport equation for each $\overline{u_i' u_j'}$ component and the dissipation rate ε. Historically, these models have difficulties to accurately predict the region near the wall, however the elliptic blending formulation of Manceau [20] (EB-RSM) is able to operate in wall-resolved meshes. Buoyancy effects are included as well as production terms by Dehoux et al. [12]:

$$\mathcal{P}_{bR_{ij}} = -\beta \left(g_i \overline{u_j' T'} + g_j \overline{u_i' T'}\right) \tag{9}$$

$$\mathcal{P}_{b\varepsilon} = C_{\varepsilon 3} \frac{\sqrt{Pr}}{\sqrt{R}} \frac{\mathcal{P}_{bk}}{\tau} \tag{10}$$

2.3. RANS turbulent heat flux modelling

The turbulent heat fluxes introduce the effects of turbulence in the mean energy equation. In most of the numerical codes, the $\overline{u_i'T'}$ components are retrieved using the Simple Gradient Diffusion Hypothesis (SGDH), an analogous of the Boussinesq assumption of Eq. (5):

$$\overline{u_i'T'} = -\alpha_t \frac{\partial \overline{T}}{\partial x_i} \tag{11}$$

where the turbulent heat fluxes are computed from the mean temperature field and the turbulent thermal diffusivity or eddy diffusivity α_t. The thermal diffusivity α_t is often related to the eddy viscosity ν_t and the turbulent Prandtl number Pr_t following the expression:

$$Pr_t = \frac{\nu_t}{\alpha_t} \tag{12}$$

The approach of Eq. (12) is widely accepted in all the CFD community because of its reasonable accuracy for Prandtl numbers close and larger than unity for $Pr_t \approx 0.85 - 0.9$. In such case the TFH approach is commonly named as Reynolds analogy (RA). However, the accuracy of this approach is completely case-dependent. For liquid metals, the low Prandtl number has a strong influence on the turbulent Prandtl number, which cannot be considered constant nor close to 0.85 – 0.9 [21]. The Nuclear Energy Agency (OECD-NEA) recommends the use of empirical or analytical expressions for Pr_t, whose value should be larger than unity [21]. One of the most used values is $Pr_t = 2$. This modification provides a more accurate prediction in comparison with direct numerical simulations (DNS) of forced convection flows [22,23] and measurements. Nevertheless, the Reynolds analogy can procure fair results under certain conditions, being a great help on simple flow configurations and initial flow field solutions.

One of the proposed closures by the OECD is the Kays correlation for Pr_t [24]. This approach is valid for very low turbulent Pèclet flows ($Pe_t \leq 10$). This model is likely to produce more accurate results than the Reynolds analogy at low Prandtl numbers, as turbulence effects are introduced in the Pr_t calculation through the eddy viscosity.

The use of transport equation models for the thermal fluctuations is also considered. Recently, Manservisi, Menghini and Da Vià proposed a two transport equations model [7,25,26], where the temperature variance k_θ and its dissipation rate ε_θ are computed. They are defined as:

$$k_\theta = \frac{1}{2}\overline{T'T'} \tag{13}$$

$$\varepsilon_\theta = \alpha \overline{\frac{\partial T'}{\partial x_j}\frac{\partial T'}{\partial x_j}} \tag{14}$$

The turbulent thermal diffusivity is defined as a function of k, ε, k_θ and ε_θ instead of relying on the turbulent Prandtl number. The model was developed for channel flows [7,25], pipe flows [7] and triangle rod bundles [25] at $Pr = 0.025$, however recent investigations have shown that this model can be used in other flow and Prandtl value configurations, such as backward facing steps [10], impinging jets [8] and planar jets with co-flow [9] up to $Pr = 0.71$.

However, the SGDH approach is not accurate enough when studying natural convection flows, as observed by Peeters and Henkes [27]. Using exclusively α_t and the temperature gradients limits the RANS turbulent heat flux prediction, far from the fluxes found in experiments and high fidelity simulations.

The truncation of the turbulent heat flux transport equation leads to an algebraic formulation of the turbulent heat fluxes. The so-called algebraic heat flux models (AHFM or AFM) considers thermal, mechanical and buoyant effects. This approach has been tested in natural convection cavities with $Pr = 0.71$ by Kenjereš et al. [15]. They proposed the formulation:

$$\overline{u_i'T'} = -C_\theta \tau \left(\zeta \overline{u_i'u_j'}\frac{\partial \overline{T}}{\partial x_j} + \xi \overline{u_j'T'}\frac{\partial \overline{U_i}}{\partial x_j} + \eta \beta g_i 2k_\theta \right) + C'_{\theta 1} a_{ij} \overline{u_j'T'} \tag{15}$$

This model has been adapted by Shams et al. [14,28,29] into the AHFM-NRG+ model to be able to operate in forced, mixed and natural convection. In the present work, the AHFM model uses the coefficients setup of Kenjereš et al. [15] instead of the ones of AHFM-NRG+. The coefficients of the AHFM-NRG+ are based in global Reynolds and Rayleigh numbers, while in the current flow the Rayleigh number is not fixed. During the present simulations the term $C'_{\theta 1} a_{ij} \overline{u_j'T'}$ has been neglected as the numerical stability was compromised. This issue was also reported by Shams [29].

The use of transport equations for each flux $\overline{u_i'T'}$ is considered in the present study. The elliptic blending differential flux model of Dehoux et al. (EB-DFM) has been considered [12]. This approach has been tested in forced, mixed and natural convection for $Pr = 0.71$, but not yet in lower Prandtl numbers. It follows the expression:

$$\frac{D\overline{u_i'T'}}{Dt} = P_{iT} + G_{iT} + \phi^*{}_{iT} - \varepsilon^*{}_{iT} + D_{iT}{}^{\nu} + D_{iT}{}^{t} \tag{16}$$

where $G_{iT} = -2\beta k_\theta g_i$ indicates the production of the turbulent heat flux due to buoyancy.

2.4. Previous RANS studies of NCBL

The natural convection boundary layer has been studied by means of high fidelity simulations but for Prandtl values equal or larger than 0.71 [2,30–34]. However, only a few old references are found when employing RANS simulations. To and Humphrey performed simulations with a low Reynolds $k - \varepsilon$ model and an Algebraic Stress Model (ASM) [35]. Turbulence production by buoyancy was incorporated during the simulations, as well as boundary conditions that contributes to the numerical transition to turbulence. The turbulent heat fluxes were computed algebraically. Mean velocity and temperature profiles were evaluated for large Grashof number values ($\mathcal{O}(10^{11})$) with satisfactory results for both turbulence models, and the ASM was performing slightly better. Qualitatively, the anisotropic turbulence was in agreement by using the ASM, however further comparisons with experiments were demanded because of discrepancies between simulations and experiments in terms of reference velocity, temperature and turbulent quantities ($\overline{u'v'}$, $\overline{v'T'}$). Henkes and Hoogendoorn employed the SGDH approach, where the turbulent heat fluxes exclusively depend on the temperature gradient [36]. They used several low Reynolds $k - \varepsilon$ models, as well as the standard one, in large Grashof values, too. Henkes stated that low Reynolds formulations are needed in order to appropriately resolve the heat transfer near the wall. Peeters et al. added to the RANS modelling of this flow a differential model for Reynolds stresses (RSM) and turbulent heat fluxes (DFM), and compared its results against an ASM and a low Reynolds $k - \varepsilon$ model [27]. It was shown that the isotropic eddy viscosity models are inadequate as the NCBL is strongly anisotropic, and therefore the need of a DFM to predict this flow. These three works date from the beginning of the 90's, and since then RANS modellers focused on natural convection confined flows [15,19,37–39].

3. Numerical configuration

3.1. Flow description

In this work, the turbulent region of the NCBL is simulated through the 2D computational domain of Fig. 3.

At the inlet patch, profiles for each field has been employed, ensuring a turbulent inflow. These profiles are obtained from the Large Eddy Simulations (LES) of the author [34]. At the wall, a no slip condition is imposed for velocity, and a constant value T_w for temperature. No wall functions are considered for k, ε, k_θ or ε_θ as the mesh is wall-resolved. The outlet patch allows the fluid to leave the computational domain, but the fluid re-entrainment is restricted. A zero gradient condition is imposed for temperature and turbulent variables. The fluid leaving

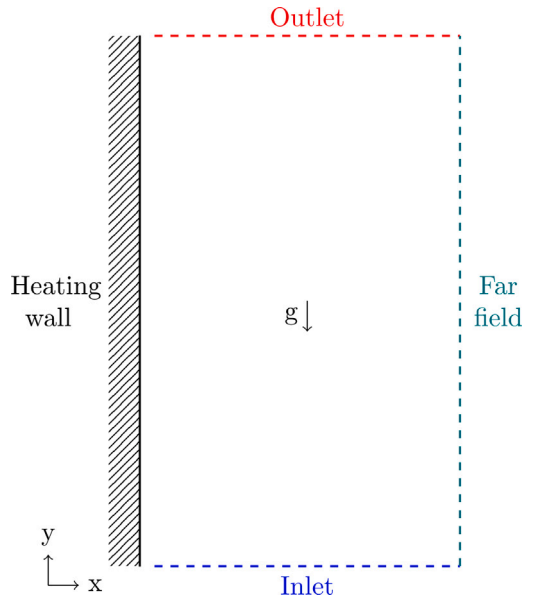

Fig. 3. Computational domain for the proposed simulations.

Table 1
Dimensionless domain size per Prandtl number. $L_i^* = L/L_b$, $L_b = (g\beta\Delta T)^{-1/3}\nu^{2/3}$.

Pr	L_x^*	L_y^*
0.71	3920	5006.54
0.2	3920	7648.46
0.025	3920	15290.98

the domain at the outlet is recirculated through the inlet and the far field patches. The incoming mass flow from the far field patch $\dot{m}_{ff}$ is obtained by the expression:

$$\dot{m}_{ff} = \dot{m}_{outlet} - \dot{m}_{inlet} \tag{17}$$

where the mass flow is based on the density, velocity and area per face on each patch. A constant temperature T_∞, lower than T_w, is considered for the fluid entering the domain through this patch. The OpenFOAM `fixedFluxPressure` boundary condition is used for pressure at the inlet, outlet and wall patches,[1] while a fixed mean value is imposed at the far field.

The dimensions for each Prandtl number simulation are indicated in Table 1. While the same normalwise length L_x^* is considered for all the Prandtl number values, the streamwise length L_y^* varies in order to arrive to the same turbulent Rayleigh range of $Ra = 10^{10} - 2.9 \cdot 10^{11}$, where the Rayleigh number is defined as:

$$Ra = \frac{g\beta\Delta T L_y^3}{\nu\alpha} \tag{18}$$

where $\Delta T = T_w - T_\infty$.

3.2. Numerical configuration

The present simulations have been performed using OpenFOAM-7 [40,41]. The finite volume method is used to solve the transport equations by using the SIMPLEC algorithm. Steady state simulations have been carried out, and the space discretization schemes correspond to second order central differences for diffusion terms, while the advective terms for velocity and temperature are based on a second order upwind scheme. The advective term for the different turbulent variables is discretized using a first order upwind scheme in order to ensure numerical stability.

The mesh size for each Prandtl number is presented in Table 2, based on the dimensions of the respective computational domain and the mesh sensitivity study of Appendix A. The distance to the wall of the first grid x^+ is kept below 0.1 for all the meshes.

Table 2
Number of cells per mesh in function of the simulated Prandtl number.

	$Pr = 0.71$	$Pr = 0.2$	$Pr = 0.025$
N_x	150	150	150
N_y	768	1173	2343
# cells	$115.2k$	$175.95k$	$351.45k$

Table 3
TMF-THF models pairing in the present work.

Label	TMFM	THFM
RA	LS $k-\varepsilon$	RA ($Pr_t = 0.85$)
PRT2	LS $k-\varepsilon$	RA ($Pr_t = 2$)
KAYS	LS $k-\varepsilon$	Kays correlation
KTET	LS $k-\varepsilon$	Manservisi et al. $k_\theta - \epsilon_\theta$
AHFM	LS $k-\varepsilon$	Kenjeres et al. AHFM
EBM	EB-RSM	EB-DFM

4. Results

The employed turbulence models in this work have been summarized in Table 3. Each simulation and their results will be referred to their assigned label, based on the employed TMF-THF models. The converged simulations are compared at the location $Ra = 1.28 \cdot 10^{11}$ against the experimental data of Tsuji [42,43], Churchill's correlations [44] and the LES of the authors [34,45,46].

4.1. Wall fluxes

The heat transfer along the wall is presented in Fig. 4 for all the different RANS simulations. The Nusselt number is used to evaluate the ratio between the convective and conductive heat transfer:

$$Nu = \frac{h \cdot y}{\kappa} = \frac{\partial T/\partial n|_w \cdot y}{\Delta T} \tag{19}$$

where h is the convective heat transfer coefficient, y is the coordinate along the heated wall and $\partial T/\partial n|_w$ is the normal wall temperature gradient. All the RANS calculations show an abrupt bump between $10^{10} \leq Ra \leq 3 \cdot 10^{10}$, caused by the interaction between the inlet and the wall boundary conditions. These overpredictions are damped at a further location, and simulations adopt a logarithmic regression at moderate and high Rayleigh values.

The employed THF models affect strongly the heat transfer prediction. The RA simulation stays close to the experimental data of Tsuji for $Pr = 0.71$, however its prediction overestimates the LES and Churchill reference profiles for $Pr = 0.2$ and 0.025. As in forced convection, the Reynolds analogy accuracy is strongly affected by the Prandtl number. A similar behaviour is found with the Kays correlation: this approach cannot reproduce accurately the wall heat flux for low Prandtl numbers in natural convection. At $Pr = 0.71$, the Kays correlation model provides a solution in agreement with Churchill's correlation, however the Nusselt prediction tends to be over-predicted at low Prandtl values. This correlation showed in the past a good thermal estimation in forced convection at low Pr [11,21,24], but in natural convection its performance is compromised. Considering a constant turbulent Prandtl number value $Pr_t = 2$, one can see that the Nusselt estimation is slightly larger than the Churchill correlation and

[1] The OpenFOAM documentation reads: "The fixed flux pressure BC sets the pressure gradient to the provided value such that the flux on the boundary is that specified by the velocity boundary condition" [40].

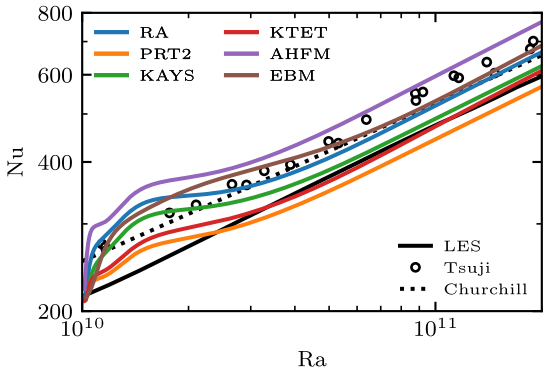

(a) $Pr = 0.71$

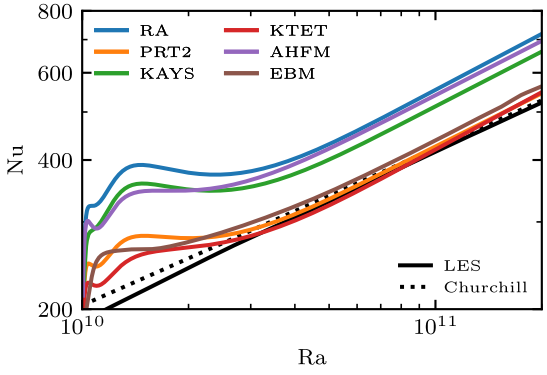

(b) $Pr = 0.2$

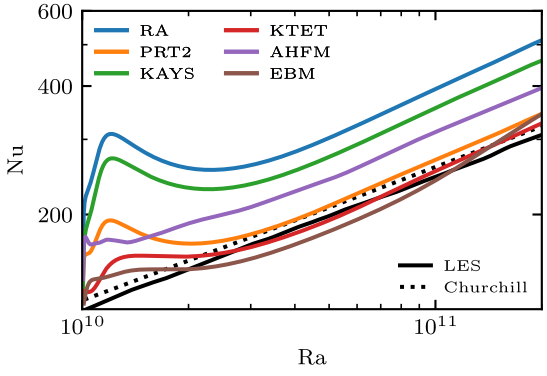

(c) $Pr = 0.025$

Fig. 4. Nusselt vs Rayleigh number along the wall.

LES profiles for $Pr = 0.2$ and 0.025. It is evident that a larger turbulent Prandtl number enhances the Nusselt number prediction for the tested three Prandtl numbers. The KTET simulations show similar results to the ones of the $Pr_t = 2$ simulation. This approach is in agreement with the reference LES profile for all the studied Prandtl numbers. Regarding the AHFM simulations, the predicted Nusselt number for $Pr = 0.71$ is fair enough with respect to the database of Tsuji. This model was assessed in confined natural convection flows at $Pr = 0.71$ [15], therefore a good estimation should be expected in unconfined flows. However at lower Prandtl numbers this THF model overpredicts by far the reference LES data and correlation. A further calibration for this model needed to improve the thermal prediction at $Pr = 0.2$ and 0.025. Nevertheless, the AHFM model provides a better Nusselt number prediction, compared with the RA and KAYS, for $Pr = 0.025$. In general, increasing the turbulent Prandtl number shows a decrease on the Nusselt number prediction, as the PRT2, KAYS and KTET simulations show with respect to the RA ones. The convective coefficient h decreases with Pr_t and reduces the wall heat flux magnitude. The opposite behaviour is found for the algebraic heat flux model as it does not introduce an extra turbulent diffusion but actually provides directly the modelled turbulent heat flux. Based in all these results, it can be concluded that in natural convection flows the chosen THF model strongly affects the flow prediction.

Using more complex turbulence models, like in the EBM simulation, enhances the Nusselt number estimation for all the three Prandtl numbers. For $Pr = 0.71$, the RANS prediction is in agreement with the experimental data of Tsuji, while the Nusselt estimation for $Pr = 0.2$ is slightly overpredicted with respect to the reference LES data and Churchill's correlation. In case of $Pr = 0.025$ the Nusselt number prediction of the differential model is the lowest one, but it can follow the reference data trends.

The wall shear stress along the wall τ_w is evaluated using the skin friction coefficient:

$$C_f = \frac{1}{2}\frac{\tau_w}{\rho_{ref} u_b^2} \tag{20}$$

where $u_b = (g\beta\Delta T\nu)^{1/3}$. The C_f evolution is presented in Fig. 5. Due to the momentum-energy coupling in natural convection, choosing an appropriate THF model is relevant in order to reproduce accurately the flow momentum. Strong C_f bumps are found around $Ra = 10^{10}$ as for the Nusselt number, but they vanish after the incoming flow gets adapted to the domain and flow conditions. These bumps present two main behaviours as a function of the employed TMF model. The Launder and Sharma $k-\varepsilon$ based simulations show a larger C_f peak value than the EB-RSM simulations. The LS model cannot predict correctly the velocity field close to the inlet region for all the three Prandtl numbers, while the EB-RSM model presents difficulties for $Pr = 0.025$. A detailed discussion on this region is provided in Appendix B.

Evaluating the skin friction after this bump is not as obvious as for the Nusselt number, though it is possible to extract relevant information. The LS $k-\varepsilon$ model provides a similar skin friction prediction for $Pr = 0.71$ when using the RA and KAYS models, which is similar to the experimental data of Tsuji. However their predictions differ when decreasing the Prandtl number. Using a value of $Pr_t = 2$ the RANS simulations improves its performance when reducing the Prandtl number. The KTET model at $Pr = 0.71$ is in a good agreement with respect to the LES skin friction coefficient. Moving into the proposed AHFM, where α_t is not considered but the turbulent heat fluxes are directly computed, the C_f is constantly overpredicted. Using the EBM configuration the skin friction prediction improves with respect to the proposed algebraic heat flux. The proposed C_f prediction is in a fair agreement with the available LES data at $Pr = 0.2$.

It can be concluded that solving the transport equations for turbulent stresses and heat fluxes improves the characterization of the wall fluxes. A further investigation on the modelled turbulent variables will lead to a better understanding of this conclusion. Regarding the initial bump C_f region, the existing TMF need to be assessed and corrected in order to correctly capture the physics coming from the reference experimental and numerical data.

4.2. Mean flow field

The velocity field is presented in Fig. 6, where the distance to the wall and the velocity value are presented by means of the law of the wall:

$$x^+ = \frac{u_\tau x}{\nu}, \quad v^+ = \frac{V}{u_\tau} \tag{21}$$

being u_τ the friction velocity at the wall. The velocity profile is divided in two regions: the inner and outer layers, separated by the maximum velocity location. The outer layer extends up to the edge of the boundary layer, where v^+ goes to zero. The inner sublayer shows two subregions: one is found very close to the wall, where $v^+ = x^+$, and

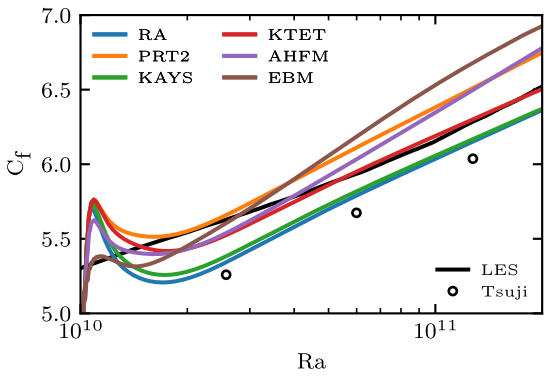

(a) $Pr = 0.71$

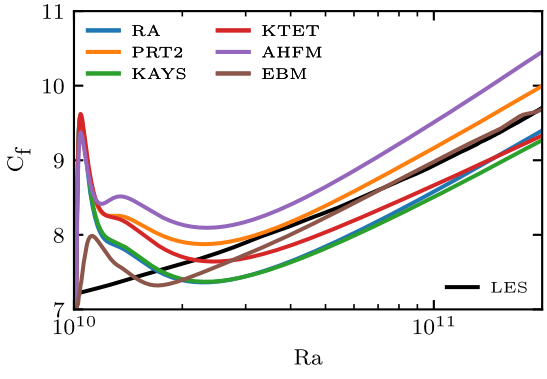

(b) $Pr = 0.2$

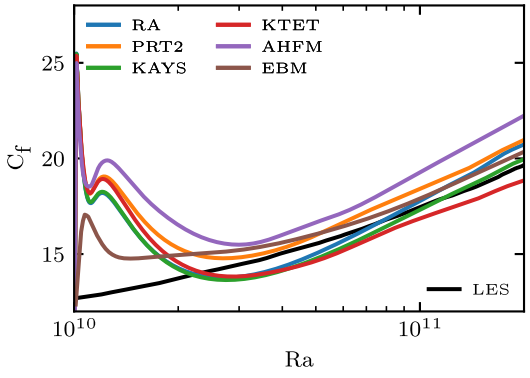

(c) $Pr = 0.025$

Fig. 5. Skin friction vs Rayleigh number along the wall.

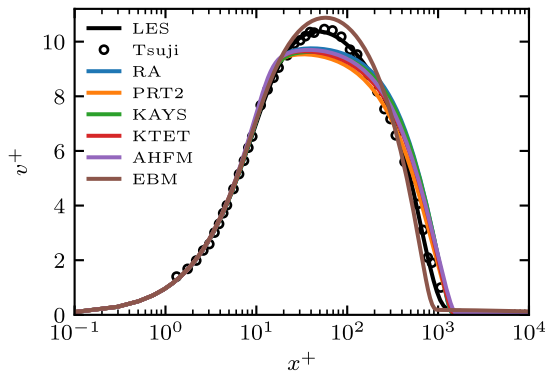

(a) $Pr = 0.71$

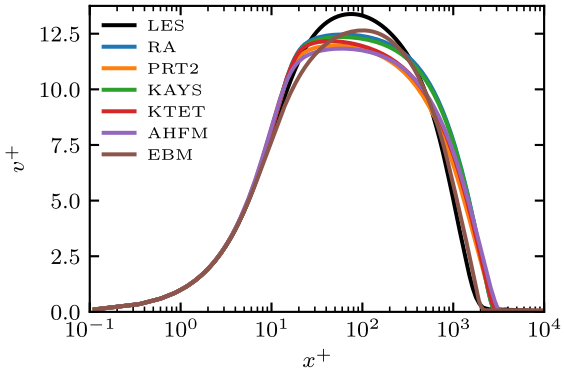

(b) $Pr = 0.2$

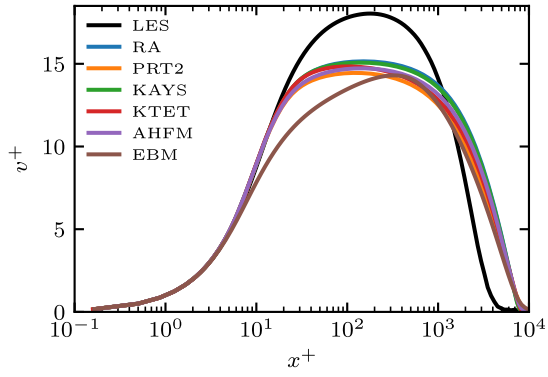

(c) $Pr = 0.025$

Fig. 6. Velocity at $Ra = 1.28 \cdot 10^{11}$.

the other extends from $x^+ \approx 5$ until the maximum velocity location. All the RANS simulations show no relevant differences on their velocity estimation in the $x^+ \leq 7$ range, which is in good agreement with the proposed reference data. Near the maximum velocity region, the RANS simulations based on the LS $k-\varepsilon$ model show an abrupt change into a flatted profile. The reached velocity peak value depends on the chosen THF model. The EBM simulation shows a good agreement with the reference data for $Pr = 0.71$ in Fig. 6(a), although the velocity peak is slightly overestimated. At $Pr = 0.2$ the differential stress model underestimates the velocity peak. This model has no significant differences on the peak magnitude at $Pr = 0.025$ with respect to the rest of simulations, however the inner region is not well captured. The prediction of the boundary layer thickness shows that using an eddy viscosity model increases the diffusion of momentum. The simulations based on the LS $k-\varepsilon$ model present a thicker boundary layer than the differential stress model for $Pr = 0.71$ and 0.2. At a very low Prandtl number no significant differences are found. If the RANS simulations are compared with the reference data it is observed that the eddy viscosity simulations always overpredict the boundary layer thickness, and the differential stress model fairly agrees with the references for $Pr = 0.71$ and 0.2.

Differences between the RANS cases are more evident in the temperature field, as seen in Fig. 7. The temperature is expressed in wall units:

$$T^+ = \frac{T_w - T}{T_\tau} \tag{22}$$

where $T_\tau = q_w / \left(\rho C_p u_\tau\right)$. The temperature profile is divided in three different regions: the inner layer, where the linear behaviour $T^+ = Pr \cdot x^+$ is found; the logarithmic layer where temperature changes are not so

Table 4
Integral deviations ϵ_U and ϵ_T between LES and RANS simulations. The lowest errors per field and Prandtl number are bolded.

Label	ϵ_U (%)			ϵ_T (%)		
Pr	0.71	0.2	0.025	0.71	0.2	0.025
RA	6.39	13.98	101.71	4.8	11.28	18.99
PRT2	6.82	17.49	66.54	4.88	2.34	5.53
KAYS	6.39	13.82	98.97	3.62	8.73	14.01
KTET	8.01	12.72	63.66	**1.94**	**1.41**	**2.80**
AHFM	8.31	15.79	78.39	11.30	12.73	12.82
EBM	**2.61**	**7.16**	**38.65**	7.42	4.52	5.06

strong; and the freestream region, where temperature remains constant. The beginning of this last region coincides with the edge of the boundary layer. Once the temperature is constant, no buoyancy effects are found and therefore the boundary layer ends in that location. As for the velocity field, the region close to the wall is coherent between the RANS and the proposed references. However, the THF model choice affects notoriously the temperature at the logarithmic and freestream regions. The RA model is in agreement with the logarithmic region of the Tsuji temperature profile at $Pr = 0.71$, and slightly overestimates the T^+ at the freestream region. It always stays far from the LES reference data, and this difference is accentuated when decreasing the Prandtl number. The Kays correlation provides larger T^+ values compared to the RA results, but they locate far from the LES. This correlation is not able to reproduce the temperature field at low Prandtl numbers, as it was found in the Nusselt number prediction. The Kays correlation cannot deal appropriately with natural convection flows at low Prandtl number. Increasing the turbulent Prandtl number up to 2 shows an overprediction on the logarithmic and freestream regions at $Pr = 0.71$ with respect to the reference LES data. However, a better thermal prediction at $Pr = 0.2$ is observed, while an acceptable estimation is found for $Pr = 0.025$. The KTET model provides reasonable temperature fields for all the three Prandtl numbers with respect to the LES reference data. The AHFM model presents the lowest T^+ values for $Pr = 0.71$, below the Tsuji experimental data. At $Pr = 0.2$, this AHFM and KAYS approaches provide a similar freestream value. The prediction of the AHFM model is still far from the reference LES data at $Pr = 0.025$, but the obtained profile is better than both RA and KAYS models. The EBM configuration shows a good overall performance for all the three Prandtl numbers, specially at $Pr = 0.2$ and 0.025. This fact is surprising as the model was only validated for $Pr = 0.71$ forced convection flows. The Prandtl number strongly affects the near wall distribution, diffusion and dissipation terms of the turbulent heat flux transport equation of the EB-DFM [12]. These contributions help to increase the turbulent heat flux in the boundary layer, and therefore the temperature diffusion by turbulence effects is enhanced. A low Prandtl number leads to a magnification of this phenomenon.

A quantitative analysis of the existing deviation between the LES and RANS profiles is carried out by means of the integral deviation:

$$\epsilon_\phi\left(x^+\right) = \left| \frac{\phi_{LES}\left(x^+\right) - \phi_{RANS}\left(x^+\right)}{\phi_{LES}\left(x^+\right)} \right| \tag{23}$$

$$\epsilon_\phi = \frac{1}{\delta}\int_0^\delta \epsilon_\phi\left(x^+\right) dx^+ \tag{24}$$

where ϕ is the integrated field along the x^+ direction between the wall and the boundary layer edge δ. A logarithmic scale has been employed to integrate the error along the integral direction to avoid data bias near the wall. A summary of the computed errors per each TMF-THF pair is found in Table 4. Considering the eddy viscosity simulations, the LS model shows difficulties to accurately predict the velocity field, regardless the chosen THF model. Using a constant turbulent Prandtl number of $Pr_t = 2$ or the proposed $k_\theta - \epsilon_\theta$ model improves the velocity prediction at $Pr = 0.025$, but their error is still far from the value

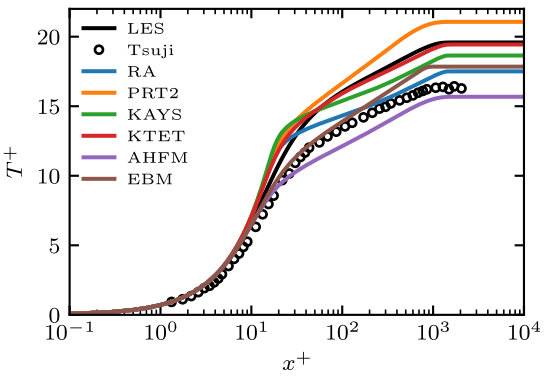

(a) $Pr = 0.71$

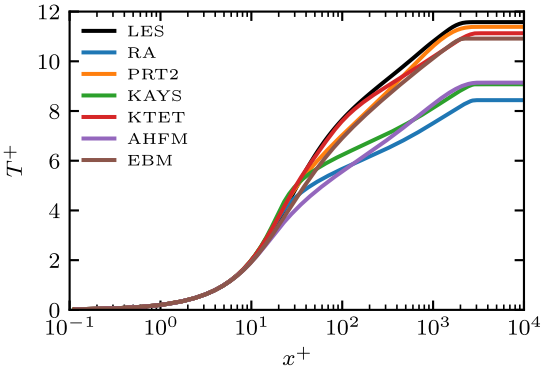

(b) $Pr = 0.2$

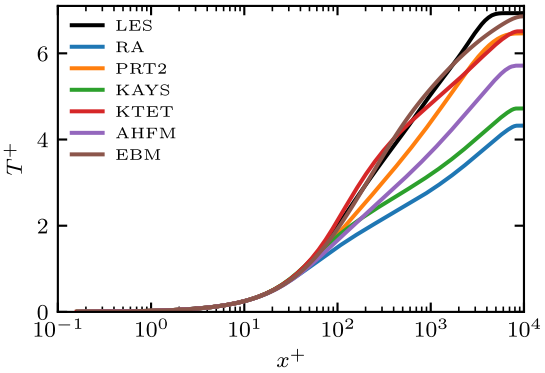

(c) $Pr = 0.025$

Fig. 7. Temperature at $Ra = 1.28 \cdot 10^{11}$.

of the EBM simulation. The output of the employed eddy viscosity model is crucial to understand its poor performance. The velocity prediction is improved using transport equations for $\overline{u_i' u_j'}$ and $\overline{u_i' T'}$, and the temperature prediction is also acceptable for all the three proposed Prandtl numbers. Despite the differences in the underlying modelling, there are two SGDH models ($Pr_t = 2$ and $k_\theta - \epsilon_\theta$) that provide a good temperature prediction together with the EBM approach. As equal as in forced convection, using a turbulent Prandtl $Pr_t = 2$ or the two equations model $k_\theta - \epsilon_\theta$ is a good choice for natural convection flows at $Pr = 0.025$.

A further investigation is mandatory to fully understand the similar performance between the proposed SGDH and the EB-DFM models.

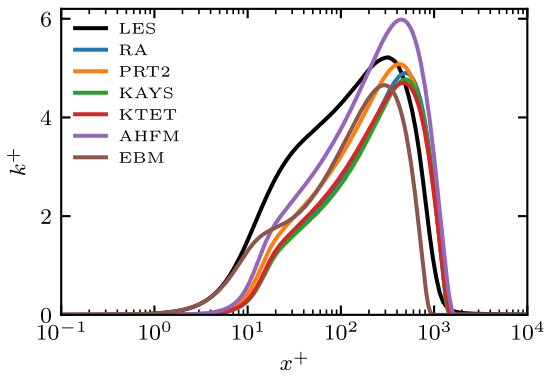

(a) $Pr = 0.71$

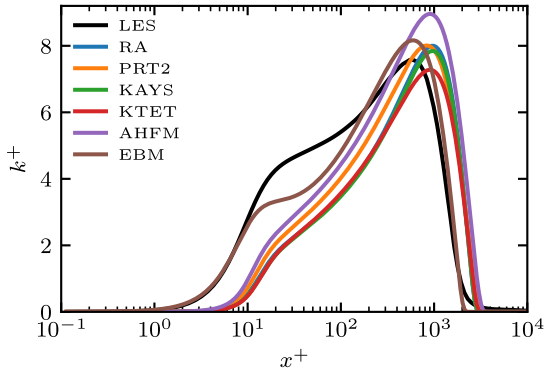

(b) $Pr = 0.2$

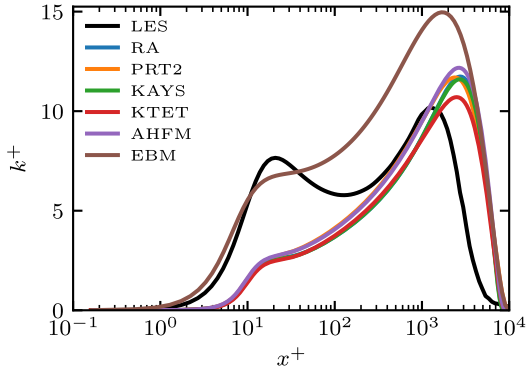

(c) $Pr = 0.025$

Fig. 8. Turbulent kinetic energy at $Ra = 1.28 \cdot 10^{11}$.

4.3. Momentum turbulent fields

The previous mean velocity and temperature fields are strongly affected by turbulence. The possible TMF-THF model combinations cause differences not only on the mean flow but also on the turbulent variables. The turbulent kinetic energy k is presented in Fig. 8 in non-dimensional form $k^+ = k/u_\tau^2$ and compared against the available LES data.

Three regions are differentiated: the inner region, where a linear correlation between x^+ and k^+ is found, an intermediate one in between the inner region and the largest k^+ peak location, and the outer region, where the turbulent kinetic energy tends to zero as the boundary layer edge approaches. The inner region is not well predicted by the LS $k-\varepsilon$ simulations when compared to the LES reference data. Only the turbulent kinetic energy obtained by the EB-RSM model growths similarly to the reference profile. For $Pr = 0.71$ and 0.2 the RANS simulations have difficulties to reproduce the intermediate region. They cannot produce enough turbulent kinetic energy. Between the eddy viscosity simulations, the one combined with the AHFM provides large k^+ values for $Pr = 0.71$ and 0.2. The buoyant production of k^+ (Eq. (7)) gets maximized when the turbulent heat flux follows the gravity direction. An investigation on the $\overline{u_i'T'}$ calculation might explain the problems when characterizing the turbulent kinetic energy. In the case of the EBM simulation, an overproduction of k^+ is found at a low Prandtl number. The buoyant production term on the Reynolds stress transport equation of Eq. (9) is used by Dehoux to include buoyant effects in the modelled velocity–pressure correlation term in Manceau's model [12]. This consideration introduces an additional contribution to the Reynolds stress transport equation, which must be reviewed for very low Prandtl numbers. The outer region shows that the employed TMF model has an effect in the boundary layer thickness. Employing the $k-\varepsilon$ model leads to an overestimation of the turbulent kinetic energy at the outer region, while the EB-RSM shortens the boundary layer thickness. This feature shows a high sensitivity to the Prandtl number: at low Prandtl numbers the boundary layer thickness is independent of the chosen turbulence closure.

The dissipation rate of the turbulent kinetic energy is presented in Fig. 9 in wall units: $\varepsilon^+ = \varepsilon/(u_\tau^4/\nu)$.

Due to the near wall treatment of the LS model, none of the $k-\varepsilon$ simulations can retrieve the ε^+ behaviour close to the wall. The Launder and Sharma model introduces blending functions and extra terms in order to retrieve the near wall behaviour close to the wall in forced convection flows. Employing them in natural convection introduces relevant discrepancies that affects the flow prediction. Far from the wall $x^+ \approx 20$ these blending functions have no effect and the natural ε behaviour is retrieved. This is not the case when using the EBM configuration: the ε estimation close to the wall is different from zero. A fair prediction is found for this simulations close to the wall and $Pr = 0.71$ and 0.2, while a large dissipation ε^+ is found at a Prandtl number $Pr = 0.025$. Far from the wall ($x^+ > 10$), all the RANS simulations follow the same trend than the LES but they always introduce a slightly larger dissipation until the end of the boundary layer. The chosen THF model has a slight effect on the ε^+ profile, but the differences on their predictions decrease with the Prandtl number.

The output of the Launder and Sharma model is the eddy viscosity ν_t, which is added in the momentum equation (Eq. (3)) with a diffusive role due to the effects of turbulence. Fig. 10 presents the non-dimensional ${\nu_t}^+ = \nu_t/\nu$ retrieved by the employed $k-\varepsilon$ model and the reference LES data. In general terms, it is found that the computed eddy viscosity yields to a continuous function while an asymptotic discontinuity is found in the LES data at the velocity peak location. At that position the velocity gradient is zero and deriving the value of the eddy viscosity from Eq. (5) generates an indeterminate expression. After this discontinuity the LS model overpredicts the eddy viscosity with respect to the LES reference until the end of the boundary layer, where $\nu_t \to 0$. The most worrying issue on the eddy viscosity prediction is the extreme overestimation of ${\nu_t}^+$ within the boundary layer. The difference between the reference LES data and the computed eddy viscosity is accentuated when decreasing the Prandtl number. This large amount of extra diffusion in the momentum equation is the responsible of the inaccurate velocity profile and the thickening of the boundary layer found on Fig. 6.

In natural convection flows both the momentum and temperature equations are coupled by buoyancy. A bad prediction of the velocity field, specially at $Pr = 0.025$, is usually associated with a wrong temperature prediction in forced convection. However, despite the lack of accuracy in the eddy viscosity calculation of the $k-\varepsilon$ model, the PRT2 and KTET approaches provide a fair temperature estimation. Regarding the EBM model, a fair prediction on the turbulent momentum fields is obtained for $Pr \geq 0.2$ but the velocity prediction get worse when decreasing the Prandtl number, though a good temperature estimation

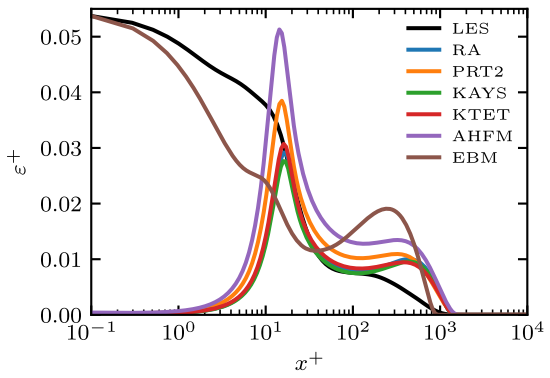

(a) $Pr = 0.71$

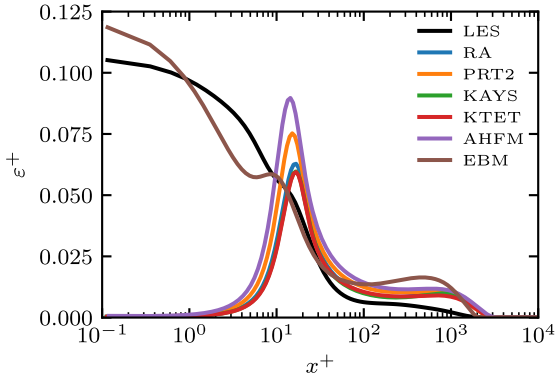

(b) $Pr = 0.2$

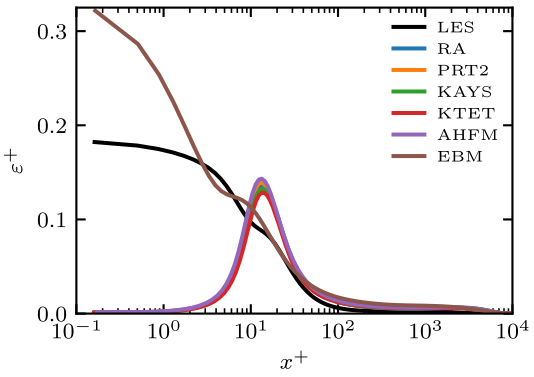

(c) $Pr = 0.025$

Fig. 9. Dissipation of turbulent kinetic energy at $Ra = 1.28 \cdot 10^{11}$.

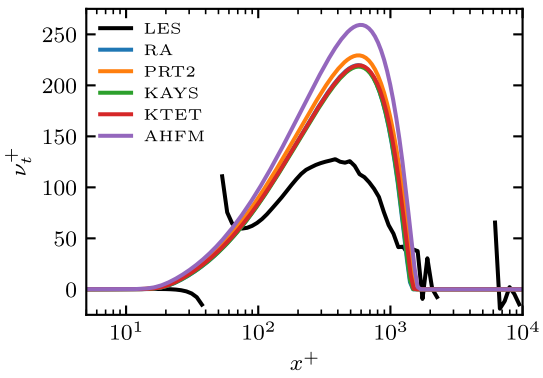

(a) $Pr = 0.71$

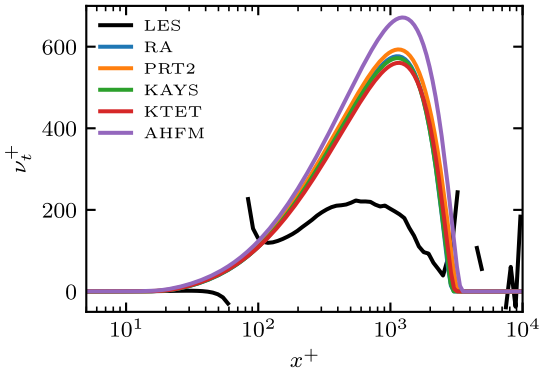

(b) $Pr = 0.2$

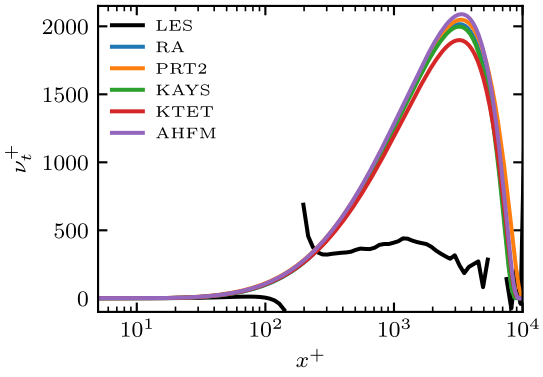

(c) $Pr = 0.025$

Fig. 10. Eddy viscosity at $Ra = 1.28 \cdot 10^{11}$.

is found. These THF models somehow counter the effects of the badly captured momentum in the temperature prediction. Studying the output of the proposed THF models is therefore needed to fully understand this phenomenon.

4.4. Thermal turbulent fields

The employed SGDH models rely on the estimation of the turbulent thermal diffusivity α_t. Either a constant turbulent Prandtl number ($Pr_t = 0.85$ or 2) or the Kays correlation, the SGDH models compute α_t as a function on the eddy viscosity retrieved by the TMF model. The Manservisi and Menghini model determines α_t based on the turbulent kinetic energy and its dissipation rate instead of on the eddy viscosity. A look into Fig. 11 shows how the previous SGDH models retrieve the α_t diffusivity starting from the turbulent fields of Section 4.3. As a common behaviour, α_t starts from zero at the wall up to a maximum value at the same location where ν_t reaches its peak value. Afterwards this diffusivity coefficient decays to zero at the boundary layer edge. In the case of the RA simulations the turbulent thermal diffusivity is highly overestimated as the eddy viscosity. Increasing the turbulent Prandtl number like in the PRT2 model drastically decreases α_t, which gets close to the reference LES data. This qualitative agreement is the responsible of the fair mean temperature field prediction. The eddy viscosity overestimation affects negatively the Kays correlation estimation of Pr_t, which is completely overwhelmed by the large ν_t values, and provide a similar α_t prediction to the Reynolds analogy one. This is why both THF models provide a similar temperature estimation in Fig. 7. The KTET model always overestimates the reference LES data, however it proportionates good mean temperature estimations. Therefore there is a threshold α_t value that allows a fair agreement independently of the employed THF model.

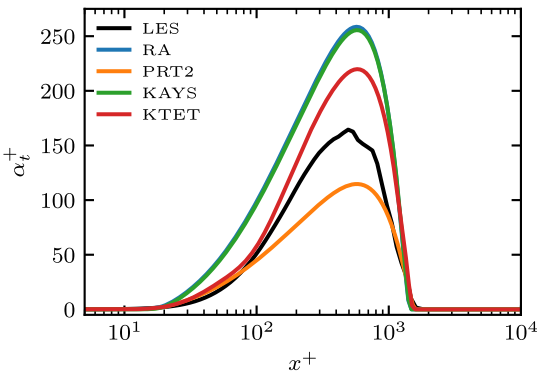

(a) $Pr = 0.71$

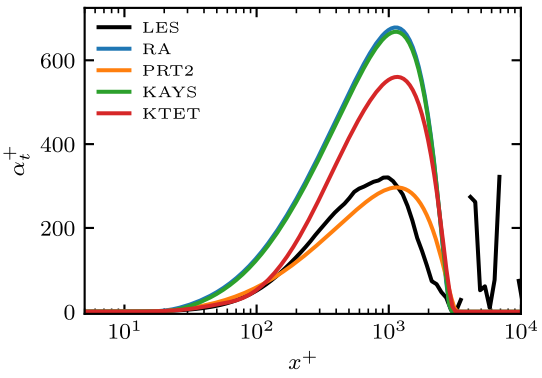

(b) $Pr = 0.2$

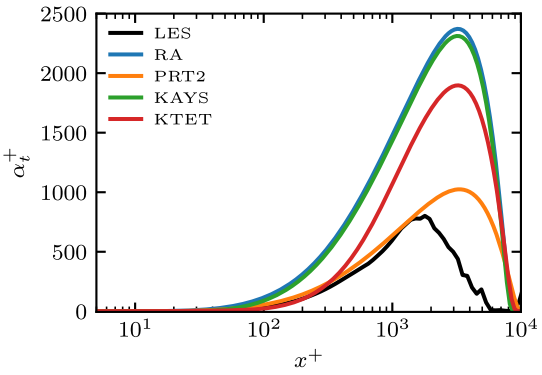

(c) $Pr = 0.025$

Fig. 11. Turbulent thermal diffusivity at $Ra = 1.28 \cdot 10^{11}$.

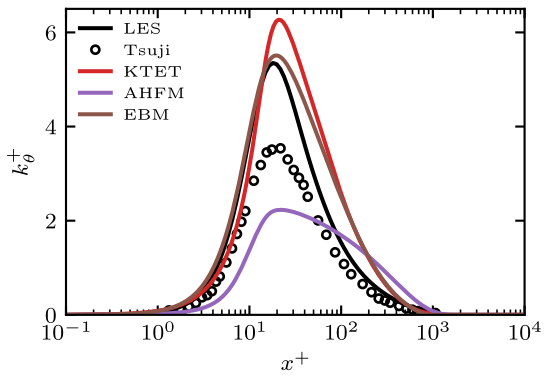

(a) $Pr = 0.71$

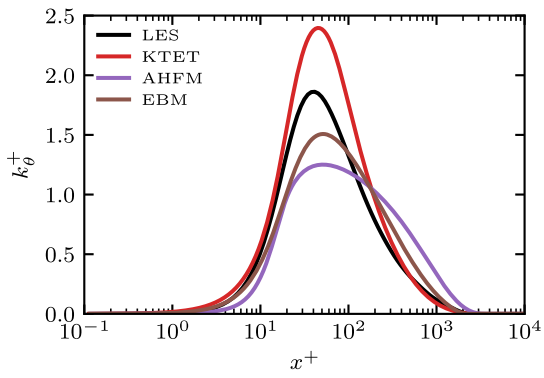

(b) $Pr = 0.2$

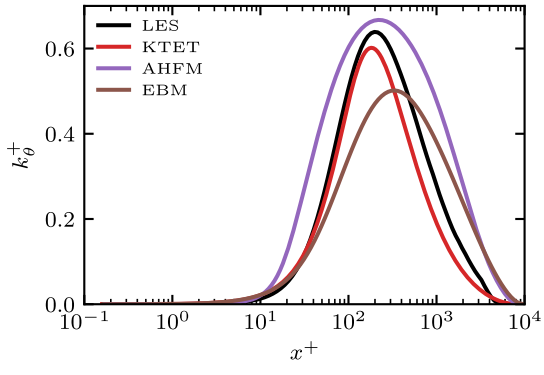

(c) $Pr = 0.025$

Fig. 12. Temperature variance at $Ra = 1.28 \cdot 10^{11}$.

The previous SGDH models do not include buoyant effects, which should be considered as well to correctly predict the turbulence effects on the flow. The temperature variance k_θ links buoyancy with the turbulent heat flux prediction of both AHFM and EB-DFM models on their respective $\overline{u_i'T'}$ modelling (Eqs. (15) and (16)), however the KTET model does not add any buoyancy contribution to the k_θ and ε_θ transport equations. The thermal variance ${k_\theta}^+ = k_\theta/T_\tau^2$ is presented in Fig. 12 for these three THF models against the proposed reference data at different Prandtl numbers. The variance is characterized by a maximum value at the edge of the inner T^+ region. Due to the constant wall temperature, k_θ tends to zero at the wall, and out of the boundary layer it comes back to zero as the temperature does not experience variations in that region. It is found that the KTET model slightly overestimates the thermal fluctuations for $Pr = 0.71$ and 0.2, specially the maximum ${k_\theta}^+$ region and the posterior decay, while a very good agreement is found for 0.025. Although this model was tuned in forced convection flows at $Pr = 0.025$, its use in natural convection retrieves a good thermal variance estimation. Regarding the AHFM model, its thermal variance characterization becomes more accurate with respect the reference data at very low Prandtl number. This model shows a strong k_θ diffusion along the boundary layer, thus its maximum values for $Pr = 0.71$ and 0.2 cannot reach the experimental nor numerical reference profiles. It is found that this model relies on the ν_t prediction, which has shown several deficiencies. The extreme large ν_t values of Fig. 10 are therefore affecting differently both the k_θ–ε_θ and the AHFM models. In the case of the EB-DFM a good temperature variance is found for $Pr = 0.71$, however for lower Prandtl numbers this approach underestimates the reference ${k_\theta}^+$ data.

The KTET, AHFM and EB-DFM models solve the transport equation of the temperature variance, however these models estimate differently the turbulent diffusion and dissipation. In terms of the turbulent

diffusion, the KTET model depends on α_t [25], the AHFM relies on ν_t [15] and the EB-DFM model on the Reynolds stresses [12]. As it has been presented before, the Launder and Sharma model present several problems when estimating the eddy viscosity. The peak value k_θ provided by the AHFM coincides with the eddy viscosity growing region (Fig. 10), increasing the diffusive effects and providing a positive balance in the k_θ transport equation. The thermal variance slowly tends to zero at large Prandtl numbers, however the eddy viscosity only introduces a negative balance during the k_θ decay. The production–dissipation relation is therefore leading the smooth thermal variance decay for $Pr = 0.71$ and 0.2. When using the two equations KTET model the turbulent diffusion is retrieved by using the turbulent thermal diffusivity α_t. The fair qualitative agreement between the reference LES data and the KTET model points that the transport equation of the thermal variance should not rely on ν_t. In the case of the EB-DFM model the turbulent diffusion is considered by using the Reynolds stress. This approach is a good approximation as found on the thermal variance results of Fig. 12 and also introduces anisotropic effects. A coefficient calibration is needed to correctly predict the thermal variance for several low Prandtl numbers.

The dissipation rate of the thermal variance ε_θ is presented in Fig. 13, where it is expressed as $\varepsilon_\theta{}^+ = \varepsilon_\theta/(u_\tau^2 T_\tau^2/\nu)$. From the LES one can see that the $\varepsilon_\theta{}^+$ value close to the wall is constant, but the RANS simulations cannot capture this trend. Both AHFM and EB-DFM models estimate the dissipation rate based on the momentum and thermal turbulent time scale ratio R. The expression of such ratio depends on the elliptic blending of Dehoux et al. in the case of the EB-DFM model [12]. Although at the original AHFM formulation several approaches for this ratio are provided [15], the simple approach $R = 0.5$ is used as it has shown reasonable results in the past according to the work of Shams on his AHFM formulation [14]. The KTET model provides a transport equation for this turbulent field, thus the time scale ratio is calculated instead of modelled. The dependency of the AHFM model on the dissipation rate ε is notorious, where the dissipation ε_θ goes to zero at the wall as the turbulent dissipation ε does. In the case of the KTET model this dependency on the ε estimation is not as relevant as in the previous case. A non-zero value is found close to the wall, however this estimation is far from the reference LES data and worsen when lowering the Prandtl number. The dissipation rate provided by the EB-DFM is in fair agreement with the reference data close to the wall for $Pr = 0.71$ and 0.2, however at a very low Prandtl number this model overestimates the expected dissipation. When moving far from the wall a peak region is found as equal as for the dissipation of turbulent kinetic energy ε. After that peak all the three THF models provide a similar dissipation profile until reaching the boundary layer edge.

The output of a THF model are the turbulent heat fluxes, independently on how they are modelled. Fig. 14 collects the turbulent heat flux $\overline{u'T'}$ on the wall normal direction for all the tested Prandtl numbers.

It is expressed function of the friction velocity and temperature $\overline{u_i'T'}^+ = \overline{u_i'T'}/(u_\tau T_\tau)$. The turbulent heat flux is almost negligible close to the wall as due to the very low levels of turbulence in this region. When leaving the wall region the $\overline{u'T'}$ heat flux suddenly increases until reaching its maximum value, and then it decays as approaching the boundary layer edge. The AHFM and EBM models have a faster response than the tested SGDH models. Therefore the $\overline{u'T'}$ estimation close to the wall needs the contribution of mechanical and buoyant effects in addition to the thermal effects. The $\overline{u'T'}$ heat flux component becomes relevant for these two models at a shorter distance to the wall for $Pr = 0.71$ and 0.2. A good prediction is provided by these two models in that region for $Pr = 0.71$, while a slight overestimation of $\overline{u'T'}$ is found for $Pr = 0.2$. In the case of the lowest Prandtl number there is not such a clear difference between the SGDH approaches compared to the AHFM and EB-DFM models. Regarding the maximum $\overline{u'T'}$ region, the constant $Pr_t = 2$ value approach is always close

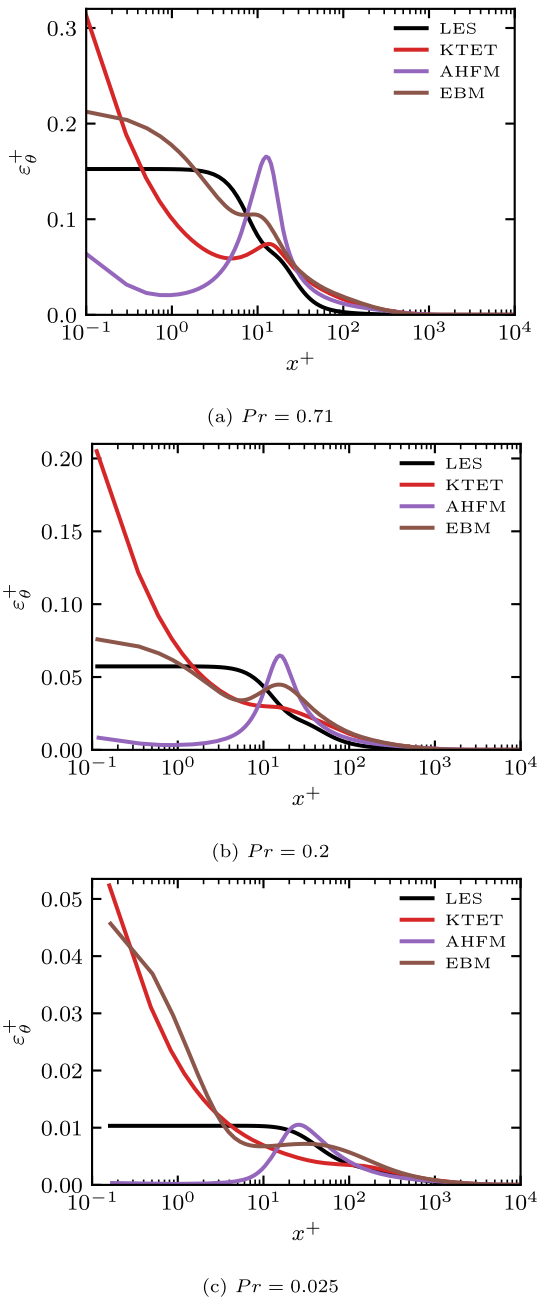

Fig. 13. Dissipation rate of the temperature variance at $Ra = 1.28 \cdot 10^{11}$.

to the reference data for all the Prandtl numbers, followed by the KTET and the EBM models. Both RA and KAYS always overestimate the expected turbulent heat flux in this region, and the AHFM model provides prediction in between the reference data and the computed RA profile.

The appropriate prediction $\overline{u'T'}$ of the SGDH models is based on its dependency on the normalwise temperature gradient. However, due to the nature of these models, the streamwise turbulent heat flux $\overline{v'T'}^+$ is almost negligible, as shown in Fig. 15. The temperature gradient is almost zero in the streamwise direction and therefore the SGDH approach cannot reproduce the LES reference data for any Prandtl number value according to Eq. (11). Only the AHFM and EB-DFM models show non-zero values as the turbulent heat flux depends not only on the temperature gradient, but also on the velocity gradient, Reynolds stresses and thermal fluctuations, which do not tend to zero

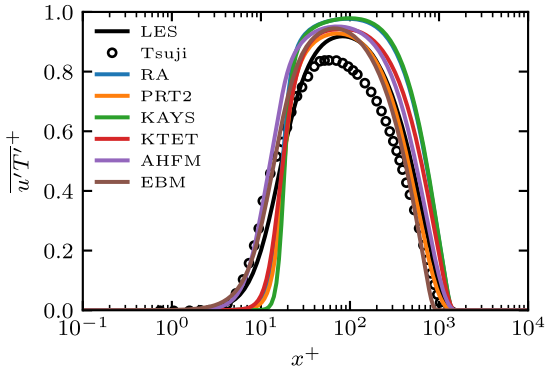

(a) $Pr = 0.71$

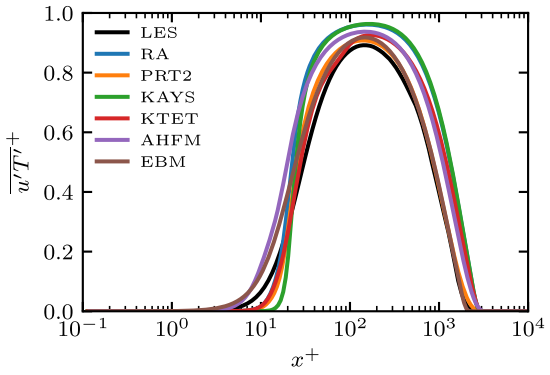

(b) $Pr = 0.2$

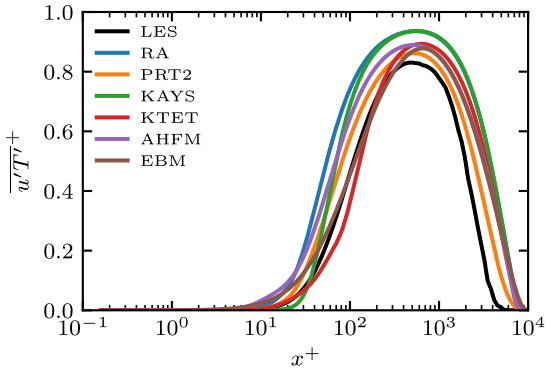

(c) $Pr = 0.025$

Fig. 14. Normalwise turbulent heat flux at $Ra = 1.28 \cdot 10^{11}$.

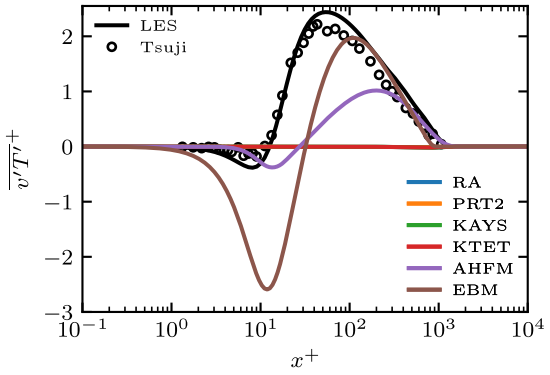

(a) $Pr = 0.71$

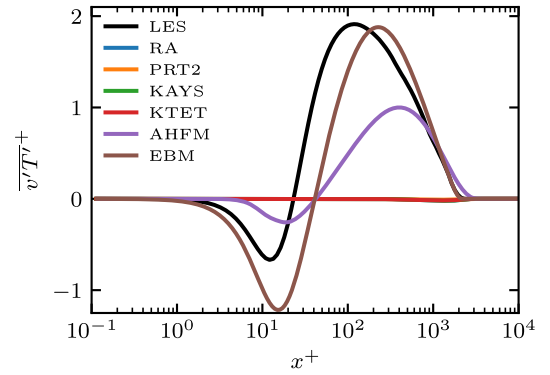

(b) $Pr = 0.2$

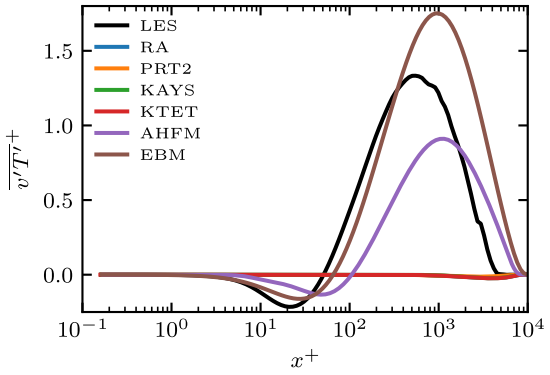

(c) $Pr = 0.025$

Fig. 15. Streamwise turbulent heat flux at $Ra = 1.28 \cdot 10^{11}$.

within the boundary layer. The poor turbulent kinetic energy prediction is therefore related with this problem, as only the turbulent heat flux component that contributes to the buoyant production of Eq. (7) in this flow configuration must be parallel to the gravity vector. The AHFM model introduces this buoyant contribution in the production of the turbulent kinetic energy, however it seems that this extra term is only relevant for $Pr = 0.71$ in Fig. 8. A further tune of the THF model might improve its performance at low Prandtl numbers. The streamwise turbulent heat flux presents, as equal as the normalwise component, a negligible value close to the wall. It suddenly decreases until reaching a minimum value, caused by a strong influence of buoyant and mechanical forces as deduced from Eq. (15). The turbulent heat flux suddenly increases up to a positive peak value, and finally decays to zero at the end of the boundary layer. The main differences between the AHFM and EB-DFM models are found on the magnitude of their respective predictions. The AHFM predictions never reach the positive peak, while the magnitude of the negative peak is well predicted for $Pr = 0.71$. In the other hand, the EB-DFM model overestimates by far the negative peak for $Pr = 0.71$ and 0.2, and provides a fair agreement on the positive peak.

Comparing the temperature predictions for these two models in Fig. 7 one can conclude that, having a similar $\overline{u'T'}$ prediction, the estimated streamwise $\overline{v'T'}$ flux plays a significant role when solving the energy equation. The larger values of $\overline{v'T'}$ of the EB-DFM model with

respect the AHFM one introduce large diffusive effects that are crucial to provide a fair temperature estimation. The fact that the KTET model provides a fair temperature estimation for the tested Prandtl numbers is therefore related with the overestimation of the turbulent thermal diffusivity α_t. The extra diffusion introduced by the THF model is the responsible of the correct behaviour of this model. When using the constant value of $Pr_t = 2$ as a THF model, the temperature prediction for $Pr = 0.71$ (Fig. 7(a)) is slightly overestimated as the computed turbulent thermal diffusivity is not large enough (Fig. 11(a)). At the intermediate Prandtl number $Pr = 0.2$ the similar α_t field (Fig. 11(b)) is good enough to provide a very accurate temperature field (Fig. 7(b)). The slight underestimation might be corrected by a fair prediction of the streamwise prediction. Finally, the overestimation of α_t in Fig. 11(c) ($Pr = 0.025$), due to the normalwise turbulent heat flux $\overline{u'T'}$, is not adequate to correctly reproduce the temperature field found in Fig. 7(c). Adding a non-zero streamwise turbulent heat flux in this simulation would have helped to reach a better temperature estimation. Therefore, these two SGDH models provide a fair temperature estimation, but they do so because of the massive turbulent thermal diffusivity overestimation instead of relying more complex physics as the AHFM and EB-DFM models do.

This conclusion demonstrate that advanced formulations of the turbulent heat fluxes are required to simulate natural convection flows. Simple Gradient Diffusion Hypothesis can be used but considering more physics on the THF model is highly recommended to correctly predict all the flow features. In addition, regarding low Prandtl number flows, it is concluded that the existing algebraic and differential flux models must be tuned to properly simulate such low Prandtl values. Their adjustment needs a further analysis on the existing numerical and experimental reference data. Correlating these data with the TMF-THF expressions would improve the setting of model coefficients or the addition of new terms to provide a better flow prediction in the low and high Rayleigh regions.

5. Conclusions

The present work shows the effect of choosing classical and advanced turbulence closures to simulate a natural convection boundary layer at three different Prandtl numbers. A low Reynolds $k-\varepsilon$ eddy viscosity model has been faced against an elliptic blending Reynolds stress model, while several SGDH models have been compared against an algebraic heat flux model and an elliptic differential flux model. The mean flow field prediction is affected by the chosen TMF and THF models. The velocity field shows two different evolutions according to the employed TMF model. Using the $k-\varepsilon$ model the velocity profiles are flattened while using the Reynolds stress model qualitatively follows the reference data. As a general behaviour the TMF model performance decreases with the Prandtl number. It has been shown that the $k-\varepsilon$ model has difficulties to correctly model the eddy viscosity. This turbulence model introduces a high overestimation of eddy viscosity, which enlarges the diffusion of momentum and introduces a large error on the velocity estimation. Using a Reynolds stress model improves the velocity prediction, although coefficient calibration is needed to improve its performance at low Prandtl numbers. The prediction of the turbulent kinetic energy is completely affected by the THF model, as its buoyant production term depends on the turbulent heat fluxes. When the turbulent heat fluxes are modelled based on the SGDH there is no buoyant contribution to the production of turbulence. This is caused by the negligible temperature gradient on the streamwise flow and gravity vector direction, reducing the turbulent heat flux into a single normalwise component. Algebraic or differential heat flux models provide a non-zero turbulent heat flux in that direction and therefore a better estimation of turbulence production is expected.

Despite the wrong prediction of the different turbulent fields by the SGDH, two different models based on the turbulent thermal diffusivity present an acceptable temperature prediction even at low Prandtl numbers, where the momentum field is not well estimated. One of these models is based on a constant turbulent Prandtl number $Pr_t = 2$. It presents a good overall prediction for all the three tested Prandtl numbers. This THF model relies on the eddy viscosity, which is always overestimated. This model introduces enough turbulent diffusion on the energy equation to provide a fair temperature prediction. The second model is based on solving the transport equations of the temperature variance and its dissipation rate, and it does not rely on the eddy viscosity to compute the turbulent thermal diffusivity, which is still highly overestimated. Nevertheless this large turbulent diffusion also benefits the temperature prediction despite the wrong momentum prediction. These models might be a valid option when initializing a natural convection simulation despite the lack of accuracy when considering mechanical effects on the flow prediction. Only the differential flux model is capable of retrieve fair results on the thermal fields without overwhelming the rest of temperature transport phenomena. The algebraic heat flux model is also a valid option, however it must be properly tuned to face the tested flow configuration.

Regarding the Prandtl number effect, it is observed that the momentum prediction deteriorates even when using a full Reynolds stress tensor and algebraic or differential turbulent heat flux models. They are capable of simulating natural convection flows, but they do need an extension to be used at low Prandtl numbers. The turbulent properties of NCBL and other natural convection flows must be deeply analysed (numerical or experimentally) and compare with the previous turbulence models in order to find new coefficient values or expressions that extend the models to a wider range of Prandtl numbers and flow configurations.

CRediT authorship contribution statement

Agustín Villa Ortiz: Conceptualization, Data curation, Formal analysis, Investigation, Methodology, Project administration, Resources, Software, Supervision, Validation, Visualization, Writing – original draft, Writing – review & editing. **Lilla Koloszar:** Funding acquisition, Supervision, Writing – review & editing.

Declaration of competing interest

The authors declare the following financial interests/personal relationships which may be considered as potential competing interests: Agustin Villa Ortiz reports financial support was provided by Euratom Research and Training Programme.

Data availability

Data will be made available on request.

Acknowledgements

The present work has been partially funded by the European SESAME Horizon 2020 project [654935].

Appendix A. Mesh sensitivity study

The sensitivity of the mesh is assessed by employing different mesh refinements in the same computational domain. The Launder and Sharma $k-\varepsilon$ model and the constant value of $Pr_t = 0.85$ have been used to simulate a NCBL with $Pr = 0.71$ in this mesh study, accordingly to the numerical configuration of Section 3. Five meshes have been tested, always keeping the same first cell size. The number of orthogonal cells on each direction is shown in Table A.5.

The mass flow rate and the averaged Nusselt number for each mesh is indicated in Table A.5. The first grid height x^+ is kept below 0.1 for all the tested meshes. The refinement reduces the deviation on the

calculated mass flow and the averaged Nusselt number decreases. The deviation is calculated as:

$$\epsilon_\phi = \frac{\phi_{ref} - \phi}{\phi_{ref}} \tag{A.1}$$

Figs. A.16 to A.18 show the mesh convergence of the velocity, temperature and turbulent kinetic energy fields. Only meshes 1, 4 and 5 are shown for clarity in Figs. A.16(a), A.17(a) and A.18(a). Comparing the provided velocity field for all the meshes against the most refined one, it is possible to retrieve the local deviation of Fig. A.16(b) based on Eq. (A.1). It is found that the velocity is less sensitive to mesh modifications very close to the wall ($x^+ < 1$). When leaving the linear region of the boundary layer, the error is minimized when the mesh resolution increases ($1 < x^+ < 20$). A non mesh sensitive location is found at $x^+ = 20$, where the maximum velocity region is reached. Afterwards, refined meshes enhance the velocity field prediction at the end of the boundary layer.

A similar conclusion can be obtained from the local deviation of temperature of Fig. A.17(b). At the logarithmic region of the thermal boundary layer a dense mesh is required to minimize its impact on the computed temperature field ($10 < x^+ < 1000$). The change of shape of the temperature profile ($x^+ = 20$) is highly sensitive to the mesh refinement.

The local deviation of the turbulent kinetic energy of Fig. A.18(b) shows large values close to the wall ($x^+ < 10$) as a consequence of the almost negligible values of k^+ in Fig. A.18(a). The turbulent kinetic energy prediction in that region certainly improves when refining the mesh. The same conclusion is found far from the wall ($20 < x^+$), specially at the outer region of the boundary layer ($500 < x^+$). In that location, it is found that the mesh 1 presents the largest deviations from mesh 5.

Mesh 4 is found as a good compromise between accuracy and computational cost for the considered Prandtl number and Rayleigh range. It provides the lowest deviation with respect mesh 5 in terms of mass flow and flow field characterization. Therefore, the $Pr = 0.71$ simulations have been performed using this domain discretization. The proposed meshes for lower Prandtl numbers have been obtained by following the recommendations of Grötzbach [47,48]. The turbulent structures on the momentum and thermal flow field enlarge when the fluid Prandtl number becomes small, therefore the discretization offered by a mesh valid for $Pr = 0.71$ is presumed to be valid also for $Pr = 0.2$ and 0.025 simulations. The same cells/length ratio is kept when simulating lower Prandtl values, while the computational domain length is adjusted to satisfy the required Rayleigh number. The number of cells per each Prandtl number is presented in Table 2.

Appendix B. Low Rayleigh region

The C_f behaviour found in Fig. 5 leads into an investigation on the velocity field characterization by the LS $k-\varepsilon$ and EB-RSM models. Fig. B.19 shows the LES, RA and EBM velocity contours. The wall normal distance $x^* = x/L_b$ and the Rayleigh number ranges have been

Table A.5
Mesh sensitivity results. x^+: averaged wall-distance at the first cells on the normalwise direction. $\dot{m}^* = \frac{1}{u_b L_b}\int_0^\delta \rho_k V dx$: dimensionless mass flow at $Ra = 1.28\cdot10^{10}$. $\overline{Nu}$: averaged turbulent Nusselt number along the wall. ϵ: relative deviation with respect to the most refined mesh.

	Mesh 1	Mesh 2	Mesh 3	Mesh 4	Mesh 5
N_x	75	100	125	150	200
N_y	364	512	640	768	896
$x^+ \cdot 10^3$	92.34	92.28	92.24	92.22	92.20
$\dot{m}^*$	6477	6533	6545	6549	6570
$\epsilon_{\dot{m}}$ (%)	1.41	0.57	0.39	0.33	–
$\overline{Nu}$	500.31	501.05	501.37	501.55	501.20
ϵ_{Nu} (%)	0.18	0.03	−0.04	−0.07	–

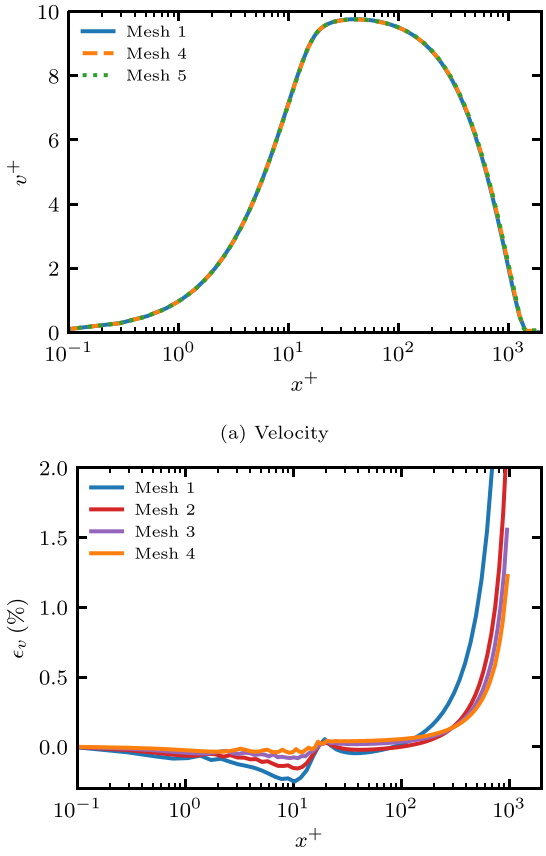

(a) Velocity

(b) Local velocity deviation

Fig. A.16. Velocity profile for meshes 1, 4 and 5 at $Ra = 1.28\cdot10^{11}$, and its local deviation from mesh 5 profile.

determined to completely observe the region of interest. These figures have been normalized with respect the local maximum velocity value found on the LES reference data. The LES contours show a velocity increase accordingly with the Rayleigh number and the boundary layer growth. When using the LS model together with any THF model, the velocity field evolves like the RA contours. The inlet velocity profile is transported a short distance before it shrinks and the velocity magnitude decreases. The velocity boundary layer presents a plateau on its peak region, accordingly to the narrowing found in $10^{10} < Ra < 2\cdot10^{10}$. After that constriction the NCBL grows again, and its magnitude and thickness increases. This behaviour is also found for the RA simulations with $Pr = 0.2$ and 0.025. The Launder and Sharma $k-\varepsilon$ laminarizes the turbulent inlet flow close to the inlet patch, and as a consequence the RANS simulations cannot reproduce the expected velocity fields of Fig. 6. The EBM simulation, which employs the EB-RSM model, does not present flow laminarization for $Pr = 0.71$. Although it does not capture accurately the velocity values for $Pr = 0.71$, the general flow pattern is correctly retrieved. For $Pr = 0.2$ and 0.025 the velocity profile shows a laminarization region at low Rayleigh values, but the velocity magnitude always stays above the RA velocity values. The EBM is therefore capable of providing a more accurate velocity boundary layer shape in Fig. 6.

The flow relaminarization is linked to the dissipation of turbulent kinetic energy. The ε contours of Fig. B.20 are normalized with respect to the local maximum ε value found on the LES reference data. It is

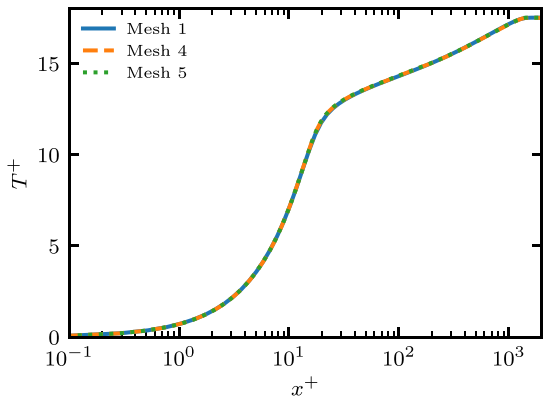

(a) Temperature

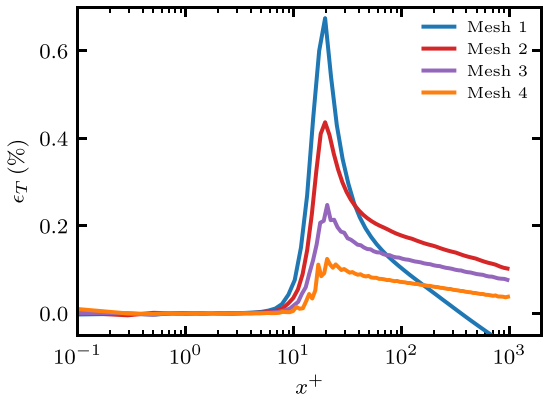

(b) Local temperature deviation

Fig. A.17. Temperature profile for meshes 1, 4 and 5 at $Ra = 1.28 \cdot 10^{11}$, and its local deviation from mesh 5 profile.

observed that the LES and EBM simulation retrieve non-zero values close to the wall unlike the RA simulation. This simulation provides a large dissipation far from the wall, near the velocity narrowing region ($0 < \log_{10} x^* < 1$), for all the Prandtl number values. The RA ϵ field shows a dissipation region around $1.5 < \log_{10} x^* < 2$ and $Ra \approx 1.5 \cdot 10^{10}$ at $Pr = 0.71$. At lower Prandtl numbers that ϵ "bubble" is diffused. The high velocity region is located in between the very large ϵ and the "bubble" regions. They subtract turbulent energy from the flow, which becomes laminar downstream. The ϵ values after $Ra > 2 \cdot 10^{10}$ decreases, and the velocity field starts increasing.

The "bubble" region is also present on the EBM simulation, and it is always located to the right of the constricted region. The near wall dissipation has also an effect on the left side of the constriction, however the EBM simulation is less sensitive to the surrounding dissipation.

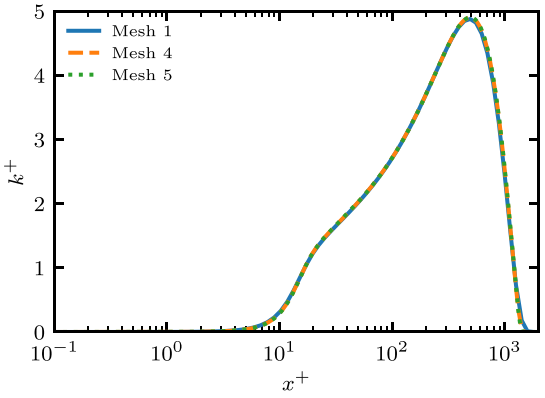

(a) Turbulent kinetic energy

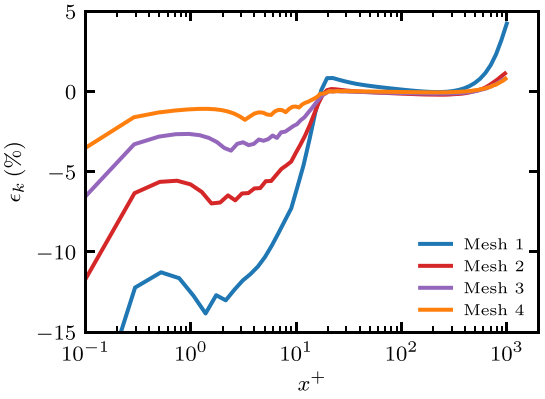

(b) Local turbulent kinetic energy deviation

Fig. A.18. Turbulent kinetic energy profile for meshes 1, 4 and 5 at $Ra = 1.28 \cdot 10^{11}$, and its local deviation from mesh 5 profile.

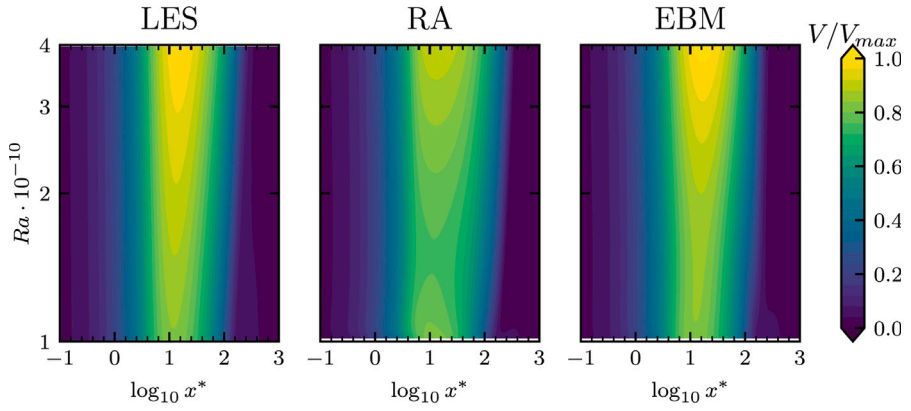

(a) $Pr = 0.71$

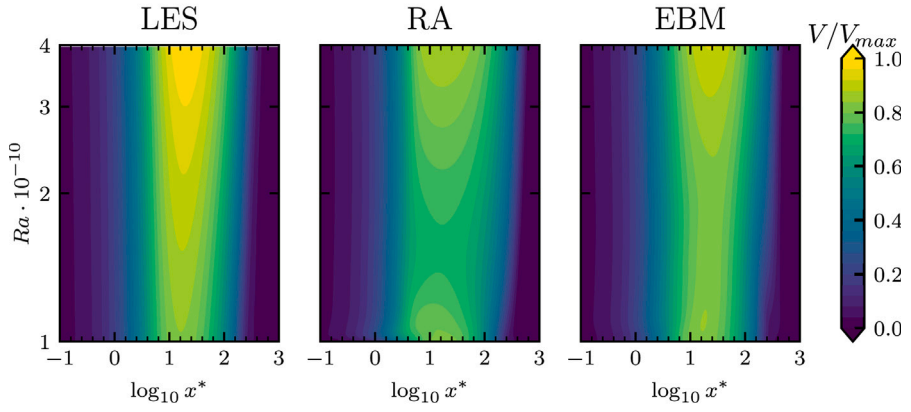

(b) $Pr = 0.2$

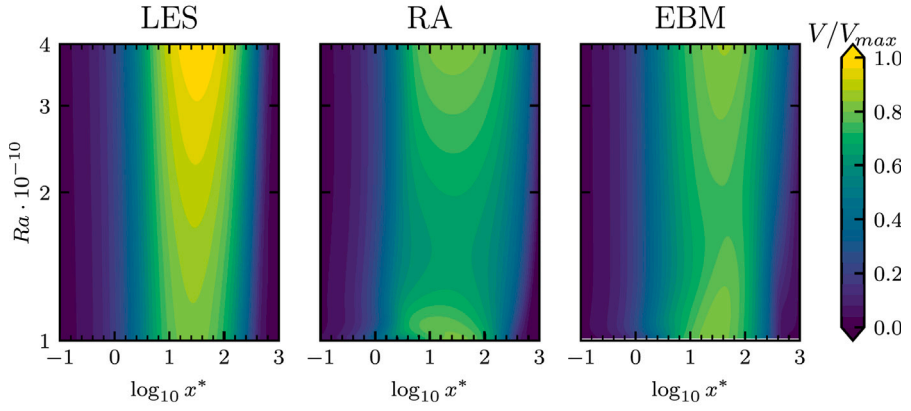

(c) $Pr = 0.025$

Fig. B.19. Velocity field for $Ra = 10^{10} - 4 \cdot 10^{10}$.

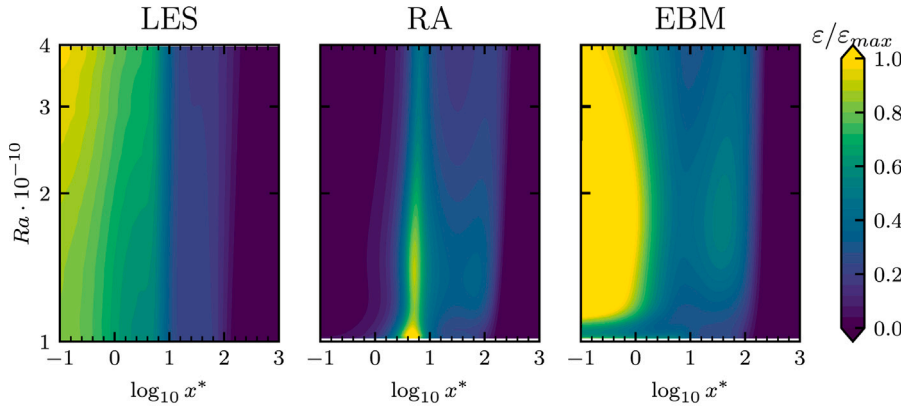

(a) $Pr = 0.71$

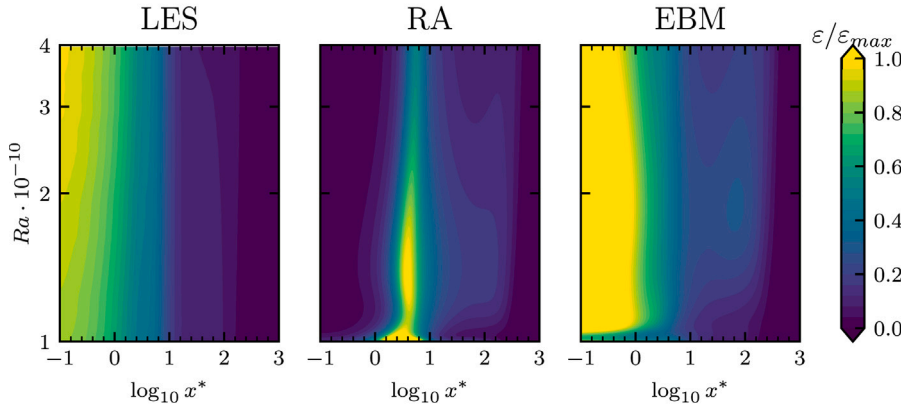

(b) $Pr = 0.2$

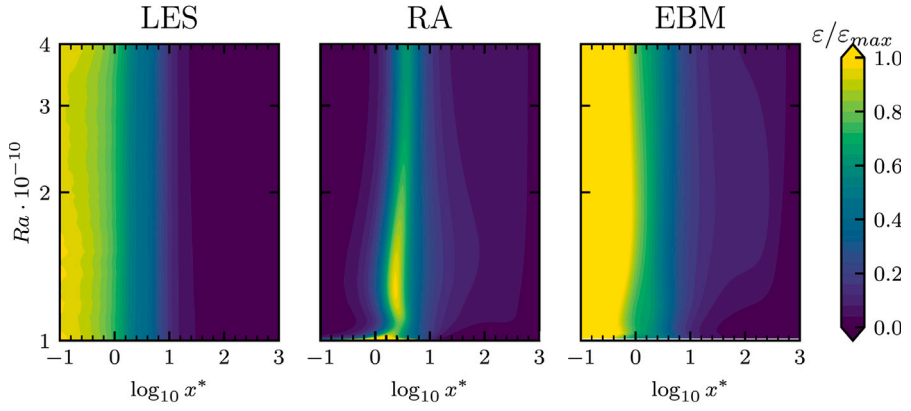

(c) $Pr = 0.025$

Fig. B.20. Dissipation rate ε field for $Ra = 10^{10} - 4 \cdot 10^{10}$.

References

[1] Bejan A. Convection heat transfer. John Wiley & Sons; 2004.

[2] Bachiri M, Bouabdallah A. An analytic investigation of the steady-state natural convection boundary layer flow on a vertical plate for a wide range of Prandtl numbers. Heat Transf Eng 2010;31(7):608–16. http://dx.doi.org/10.1080/01457630903425908.

[3] Ke H, He Y, Liu Y, Cui F. Mixture working gases in thermoacoustic engines for different applications. Int J Thermophys 2012;33(7):1143–63. http://dx.doi.org/10.1007/s10765-012-1268-z.

[4] Pacio J. Thermal-hydraulic experiments with liquid metals—Introduction. In: Thermal hydraulics aspects of liquid metal cooled nuclear reactors. Elsevier; 2019, p. 45–7. http://dx.doi.org/10.1016/B978-0-08-101980-1.00003-X, URL https://linkinghub.elsevier.com/retrieve/pii/B978008101980100003X.

[5] Garaud P. Journey to the center of stars: The realm of low Prandtl number fluid dynamics. Phys Rev Fluids 2021;6:030501. http://dx.doi.org/10.1103/PhysRevFluids.6.030501, URL https://link.aps.org/doi/10.1103/PhysRevFluids.6.030501.

[6] Roelofs F, Gerschenfeld A, Tarantino M, Van Tichelen K, D. Pointer W. Thermal-hydraulic challenges in liquid-metal-cooled reactors. In: Thermal hydraulics aspects of liquid metal cooled nuclear reactors. Elsevier; 2019, p. 17–43. http://dx.doi.org/10.1016/B978-0-08-101980-1.00002-8, URL https://linkinghub.elsevier.com/retrieve/pii/B9780081019801000028.

[7] Manservisi S, Menghini F. A CFD four parameter heat transfer turbulence model for engineering applications in heavy liquid metals. Int J Heat Mass Transfer 2014;69:312–26. http://dx.doi.org/10.1016/j.ijheatmasstransfer.2013.10.017, URL https://linkinghub.elsevier.com/retrieve/pii/S0017931013008776.

[8] De Santis A, Ortiz AV, Shams A, Koloszar L. Modelling of a planar impinging jet at unity, moderate and low Prandtl number: Assessment of advanced RANS closures. Ann Nucl Energy 2019;129:125–45. http://dx.doi.org/10.1016/j.anucene.2019.01.039, URL https://linkinghub.elsevier.com/retrieve/pii/S0306454919300465.

[9] Cascioli E, Buckingham S, Keijers S, Tichelen KV, Kenjeres S. Numerical and experimental analysis of a planar jet with heated co-flow at medium and low Prandtl-number values. Nucl Eng Des 2020;361:110570. http://dx.doi.org/10.1016/j.nucengdes.2020.110570, URL https://linkinghub.elsevier.com/retrieve/pii/S0029549320300650.

[10] Buckingham S, Shams A, Villa Ortiz A. Numerical prediction of flow and heat transfer in a Backward Facing Step at various Prandtl fluids. SESAME Final International Workshop. Petten, The Netherlands; 2019.

[11] Shams A, Roelofs F, Tiselj I, Oder J, Bartosiewicz Y, Duponcheel M, et al. A collaborative effort towards the accurate prediction of turbulent flow and heat transfer in low-Prandtl number fluids. Nucl Eng Des 2020;366:110750. http://dx.doi.org/10.1016/j.nucengdes.2020.110750, URL https://linkinghub.elsevier.com/retrieve/pii/S0029549320302442.

[12] Dehoux F, Benhamadouche S, Manceau R. An elliptic blending differential flux model for natural, mixed and forced convection. Int J Heat Fluid Flow 2017;63:190–204. http://dx.doi.org/10.1016/j.ijheatfluidflow.2016.09.003, URL https://linkinghub.elsevier.com/retrieve/pii/S0142727X16305471.

[13] Da Vià R, Manservisi S. Numerical simulation of forced and mixed convection turbulent liquid sodium flow over a vertical backward facing step with a four parameter turbulence model. Int J Heat Mass Transfer 2019;135:591–603. http://dx.doi.org/10.1016/j.ijheatmasstransfer.2019.01.129, URL https://linkinghub.elsevier.com/retrieve/pii/S0017931018341577.

[14] Shams A, De Santis A, Roelofs F. An overview of the AHFM-NRG formulations for the accurate prediction of turbulent flow and heat transfer in low-Prandtl number flows. Nucl Eng Des 2019;355:110342. http://dx.doi.org/10.1016/j.nucengdes.2019.110342, URL https://linkinghub.elsevier.com/retrieve/pii/S0029549319303772.

[15] Kenjereš S, Gunarjo S, Hanjalić K. Contribution to elliptic relaxation modelling of turbulent natural and mixed convection. Int J Heat Fluid Flow 2005;26(4):569–86. http://dx.doi.org/10.1016/j.ijheatfluidflow.2005.03.007, URL https://linkinghub.elsevier.com/retrieve/pii/S0142727X05000342.

[16] Manceau R. Modelling of turbulent natural convection. Ljubljana, Slovenia: Josef Stefan Institute (IJS); 2019, URL https://hal.science/hal-02319389/.

[17] Jameel SMS, Manceau R, Herbert V. A buoyancy extension for eddy-viscosity models for the natural convection regime. In: 17th European turbulence conference. 2019, URL https://hal.archives-ouvertes.fr/hal-02305788.

[18] Launder BE, Sharma BI. Application of the energy-dissipation model of turbulence to the calculation of flow near a spinning disc. Lett Heat Mass Transf 1974;1(2):131–7. http://dx.doi.org/10.1016/0094-4548(74)90150-7.

[19] Henkes R, Van Der Vlugt F, Hoogendoorn C. Natural-convection flow in a square cavity calculated with low-Reynolds-number turbulence models. Int J Heat Mass Transfer 1991;34(2):377–88. http://dx.doi.org/10.1016/0017-9310(91)90258-G, URL https://linkinghub.elsevier.com/retrieve/pii/001793109190258G.

[20] Manceau R. Recent progress in the development of the Elliptic Blending Reynolds-stress model. Int J Heat Fluid Flow 2015;51:195–220. http://dx.doi.org/10.1016/j.ijheatfluidflow.2014.09.002, URL https://linkinghub.elsevier.com/retrieve/pii/S0142727X14001179.

[21] NEA. Handbook on Lead-bismuth Eutectic Alloy and Lead Properties, Materials compatibility, Thermal-hydraulics and Technologies. Paris: OECD Publishing; 2015.

[22] Kawamura. DNS database of wall turbulence and heat transfer. 2009, http://murasun.me.noda.tus.ac.jp/turbulence/index.html.

[23] Kawamura H, Abe H, Matsuo Y. DNS of turbulent heat transfer in channel flow with respect to Reynolds and Prandtl number effects. Int J Heat Fluid Flow 1999;20(3):196–207. http://dx.doi.org/10.1016/S0142-727X(99)00014-4.

[24] Kays WM. Turbulent Prandtl number—where are we? J Heat Transfer 1994;116(2):284–95. http://dx.doi.org/10.1115/1.2911398, URL https://asmedigitalcollection.asme.org/heattransfer/article/116/2/284/383190/Turbulent-Prandtl-NumberWhere-Are-We.

[25] Manservisi S, Menghini F. Triangular rod bundle simulations of a CFD $\kappa-\varepsilon-\kappa_\theta-\varepsilon_\theta$ heat transfer turbulence model for heavy liquid metals. Nucl Eng Des 2014;273:251–70. http://dx.doi.org/10.1016/j.nucengdes.2014.03.022, URL https://linkinghub.elsevier.com/retrieve/pii/S0029549314001721.

[26] Da Vià R, Manservisi S, Menghini F. A $\kappa-\omega$ $\kappa_\theta-\omega_\theta$ four parameter logarithmic turbulence model for liquid metals. Int J Heat Mass Transfer 2016;101:1030–41. http://dx.doi.org/10.1016/j.ijheatmasstransfer.2016.05.084, URL https://linkinghub.elsevier.com/retrieve/pii/S0017931016307803.

[27] Peeters T, Henkes R. The Reynolds-stress model of turbulence applied to the natural-convection boundary layer along a heated vertical plate. Int J Heat Mass Transfer 1992;35(2):403–20. http://dx.doi.org/10.1016/0017-9310(92)90278-Z, URL https://linkinghub.elsevier.com/retrieve/pii/001793109290278Z.

[28] Shams A, Roelofs F, Baglietto E, Lardeau S, Kenjeres S. Assessment and calibration of analgebraic turbulent heat flux model for low-Prandtl fluids. Int J Heat Mass Transfer 2014;79:589–601. http://dx.doi.org/10.1016/j.ijheatmasstransfer.2014.08.018, URL https://www.sciencedirect.com/science/article/pii/S0017931014007054.

[29] Shams A, De Santis A. Towards the accurate prediction of the turbulent flow and heat transfer in low-Prandtl fluids. Int J Heat Mass Transfer 2019;130:290–303. http://dx.doi.org/10.1016/j.ijheatmasstransfer.2018.10.096, URL https://linkinghub.elsevier.com/retrieve/pii/S0017931018336366.

[30] Yan Z, Nilsson E. Large eddy simulation of natural convection along a vertical isothermal surface. Heat Mass Transf 2005;41(11):1004–13. http://dx.doi.org/10.1007/s00231-005-0620-2.

[31] Abedin MZ, Tsuji T, Hattori Y. Direct numerical simulation for a time-developing natural-convection boundary layer along a vertical flat plate. Int J Heat Mass Transf 2009;52(19):4525–34. http://dx.doi.org/10.1016/j.ijheatmasstransfer.2009.03.061.

[32] Abramov AG, Smirnov EM, Goryachev VD. Temporal direct numerical simulation of transitional natural-convection boundary layer under conditions of considerable external turbulence effects. Fluid Dynam Res 2014;46(4):041408. http://dx.doi.org/10.1088/0169-5983/46/4/041408.

[33] Nakao K, Hattori Y, Suto H. Numerical investigation of a spatially developing turbulent natural convection boundary layer along a vertical heated plate. Int J Heat Fluid Flow 2017;128–38. http://dx.doi.org/10.1016/j.ijheatfluidflow.2016.09.006.

[34] Villa Ortiz A, Koloszar L, Planquart P. Large Eddy Simulations on a natural convection boundary layer at Pr=0.71 and 0.025. Nucl Eng Des 2019;353:110231. http://dx.doi.org/10.1016/j.nucengdes.2019.110231, URL https://linkinghub.elsevier.com/retrieve/pii/S0029549319302493.

[35] To W, Humphrey J. Numerical simulation of buoyant, turbulent flow—I. Free convection along a heated, vertical, flat plate. Int J Heat Mass Transfer 1986;29(4):573–92. http://dx.doi.org/10.1016/0017-9310(86)90091-8, URL https://www.sciencedirect.com/science/article/pii/0017931086900918.

[36] Henkes R, Hoogendoorn C. Comparison of turbulence models for the natural convection boundary layer along a heated vertical plate. Int J Heat Mass Transfer 1989;32(1):157–69. http://dx.doi.org/10.1016/0017-9310(89)90099-9, URL https://linkinghub.elsevier.com/retrieve/pii/0017931089900999.

[37] Dol H, Hanjalić K, Kenjereš S. A comparative assessment of the second-moment differential and algebraic models in turbulent natural convection. Int J Heat Fluid Flow 1997;18(1):4–14. http://dx.doi.org/10.1016/S0142-727X(96)00149-X, URL https://linkinghub.elsevier.com/retrieve/pii/S0142727X9600149X.

[38] Hsieh K, Lien F. Numerical modeling of buoyancy-driven turbulent flows in enclosures. Int J Heat Fluid Flow 2004;25(4):659–70. http://dx.doi.org/10.1016/j.ijheatfluidflow.2003.11.023, URL https://linkinghub.elsevier.com/retrieve/pii/S0142727X03001565.

[39] Hanjalić K. One-point closure models for buoyancy driven turbulent flows. Annu Rev Fluid Mech 2002;34(1):321–47. http://dx.doi.org/10.1146/annurev.fluid.34.082801.161035, URL http://www.annualreviews.org/doi/10.1146/annurev.fluid.34.082801.161035.

[40] The OpenFOAM Foundation. OpenFOAM v7 User Guide, URL https://cfd.direct/openfoam/user-guide.

[41] Weller HG, Tabor G, Jasak H, Fureby C. A tensorial approach to computational continuum mechanics using object-oriented techniques. Comput Phys 1998;12(6):620. http://dx.doi.org/10.1063/1.168744, URL http://scitation.aip.org/content/aip/journal/cip/12/6/10.1063/1.168744.

[42] Tsuji T, Nagano Y. Characteristics of a turbulent natural convection boundary layer along a vertical flat plate. Int J Heat Mass Transfer 1988;31(8):1723–34. http://dx.doi.org/10.1016/0017-9310(88)90284-0, URL https://linkinghub.elsevier.com/retrieve/pii/0017931088902840.

[43] Tsuji T, Nagano Y. Turbulence measurements in a natural convection boundary layer along a vertical flat plate. Int J Heat Mass Transfer 1988;31(10):2101–11. http://dx.doi.org/10.1016/0017-9310(88)90120-2, URL https://linkinghub.elsevier.com/retrieve/pii/0017931088901202.

[44] Churchill SW, Chu HH. Correlating equations for laminar and turbulent free convection from a vertical plate. Int J Heat Mass Transfer 1975;18(11):1323–9. http://dx.doi.org/10.1016/0017-9310(75)90243-4, URL https://linkinghub.elsevier.com/retrieve/pii/0017931075902434.

[45] Villa Ortiz A, Koloszar L. Application of numerical transition control method to enhance turbulence in a natural convection boundary layer over a vertical heated plate. Comput & Fluids 2020;199:104417. http://dx.doi.org/10.1016/j.compfluid.2019.104417, URL https://linkinghub.elsevier.com/retrieve/pii/S0045793019303755.

[46] Villa Ortiz A. Turbulent natural convection along a vertical plate for different Prandtl number fluids. von Karman Institute for Fluid Dynamics, URL http://hdl.handle.net/2078.1/264040.

[47] Grötzbach G. Revisiting the resolution requirements for turbulence simulations in nuclear heat transfer. Nucl Eng Des 2011;241(11):4379–90. http://dx.doi.org/10.1016/j.nucengdes.2010.12.027, URL https://linkinghub.elsevier.com/retrieve/pii/S0029549311000744.

[48] Grötzbach G. Challenges in low-Prandtl number heat transfer simulation and modelling. Nucl Eng Des 2013;264:41–55. http://dx.doi.org/10.1016/j.nucengdes.2012.09.039, URL https://linkinghub.elsevier.com/retrieve/pii/S0029549313000952.